3-D Bio-inspired Microenvironments for *In Vitro* Cell Migration

Seyed Yahya Hosseini

Dissertation submitted to the faculty of the Virginia Polytechnic Institute and State University in partial fulfillment of the requirements for the degree of

Doctor of Philosophy

In

Electrical Engineering

Masoud Agah, Chair
Yong Woo Lee
Deborah Kelly
Chang Lu
Yong Xu

September 11, 2015

Blacksburg, VA

Keywords: 3-D, Microfabrication, Microsystems, Microelectromechanical Systems, Hydrogels, Cell Migration, Dielectrophoresis

3-D Bio-inspired Microenvironments for *In Vitro* Cell Migration

Yahya Hosseini

ABSTRACT

Cancer metastasis is the leading cause of death related to cancer diseases. Once the cancer cells depart the primary tumor site and enter the blood circulation, they spread through the body and will likely initiate a new tumor site. Therefore, understanding the cell migration and stopping the spread in the initial stage is the utmost of importance. In this dissertation, we have proposed a 3-D microenvironment that (partially) mimics the structures, complexity and circulation of human organs for cell migration studies.

We have developed the tools to fabricate 3-D complex geometries in PDMS from our previously developed single-mask, single-etch technology in silicon. In this work, 3-D patterns are transferred from silicon structures to glass following anodic bonding and high temperature glass re-flow processes. Silicon is etched back thoroughly *via* wet etching and the glass is used as master device to create 3-D PDMS structures for use in dielectrophoresis cell sorting applications. Furthermore, this work has been modified to fabricate 3-D master devices in PDMS to create 3-D structures in collagen hydrogels to mimic native tissue structures. We have studied the interaction of endothelial cells with model geometries of blood vessels in collagen hydrogel at different concentrations to mimic the biomechanical properties of tissues varying from normal to tumor under the growth factor stimulation. Finally, we have designed and fabricated a silicon-based transmigration well with a 30μm-thick membrane and 8μm pores. This platform includes a deep microfluidic channel on the back-side sealed with a glass wafer. The migratory behavior of highly metastatic breast cancer cells, MDA-MB-231, is tested under different drug treatment conditions. This versatile platform will enable the application of more complex fluidic circulation profile, enhanced integration with other technologies, and running multiple assays simultaneously.

To My Family

Acknowledgements

This dissertation reflects precious moments of an enjoyable collaboration with many great people during the past few years of my life in the graduate school. Throughout this work, I received the generous support of faculty members, fellow colleagues, and friends at Virginia Tech, which I cannot summarize their kindness in a few lines here.

I would like to express my gratitude to my supervisor, Dr. Masoud Agah, for giving me the opportunity to work in his research group. I am greatly indebted to him for his continuous support, patience, and enthusiasm. I gratefully thank Dr. Deborah Kelly, Dr. Chang Lu, Dr. Yong Woo Lee, and Dr. Yong Xu for reviewing my dissertation and providing helpful suggestions and critiques to improve this work. This research was supported in part by NSF, ICTAS, and NIH. I would like to thank our collaborator, Dr. Scott Verbridge, for providing his lab through the hydrogel synthesizing experiments, and providing helpful comments and suggestions. I would like extend and express my thanks to my colleagues and friends, Dr. Shree Narayanan, Dr. Vaishnavi Srinivasaraghavan, Ms. Sepeedah Soltanian-Zadeh, Mr. Hesam Babahosseini, Mr. Alperen Ketene, Mr. Mehdi Alemi, Dr. Phillip Zellner, Dr. Muhammad Akbar, Dr. Hamza Shakeel, and other past members in VTMEMS Lab, and Ms. Megan Cox, Ms. Jill Ivey, and Ms. Brittany Balhouse in Verbridge's lab who made this journey an unforgettable one. I would like to thank Mr. Aboozar Monavarfeshani for enthusiastically getting my feet wet with biology. Furthermore, I would like to thank Mr. Donald Leber, Dr. Kristi DeCourcy and Mr. Stephen McCartney for providing technical assistance for the microfabrication, characterization and metrology of this work. I also would like to thank Dr. Bob Geil at the University of North Carolina, Chapel Hill for providing technical assistance for the microfabrication work.

Last but most importantly, I sincerely appreciate the encouragement and patience my parents and sisters provided all throughout my life. I truly admire their invaluable support and love.

Yahya Hosseini
September 2015

Table of Contents

List of Figures

List of Tables

Chapter 1. Introduction

1.1 Cell invasion and migration

According to the American Cancer Society (ACS), in 2014, more than 1.6 million new cases of cancer were diagnosed only in the United States [1]. Unfortunately, the current standard treatment methods are not effective if the patients are diagnosed at late stages of cancer. With recent advancement in biotechnology, new anti-metastasis drugs have been developed to reduce the risk of cancer spread throughout the body. Such drugs are currently in human clinical trials and still used in combination with the old treatment techniques. Although the application of the new drugs have been investigational, they are promising to be a safer and non-toxic alternative to the standard chemotherapeutic approaches when their interaction with the extracellular matrix (ECM) and tumorigenic cells is fully understood. In order to better understand the effectiveness of such drugs, in addition to approved, yet complicated and lengthy, tests on human subjects, it is necessary to develop tools to perform these studies in a system that closely resembles tumor microenvironments outside human body (*in vitro* micro-devices).

Metastasis is responsible for 90% for cancer death. Metastasis involves the departure of cancer cells from the primary tumors to the spread of cells at the distance sites. As Figure 1-1 shows, in brief, during the metastasis process tumor microenvironment secretes growth factors that leads to formation of new blood vessels nearby the tumor cells (angiogenesis). Then cancer cells invade the surrounding ECM, enter the microvasculature (intravastation), and traverse through the blood stream to reach the tissues at distant sites. At the end, cancer cells exit the microvasculature (extravasation) and establish and proliferate in the new microenvironment, and this cycle may continue [2]. As already described above, metastasis involves multiple processes. However, the initial cell invasion to the ECM and tissue is the main stage where the cancer metastasis is orchestrated. Therefore, understanding the interaction of cells with the microenvironment is an utmost of importance on how it acquires invasive characteristics.

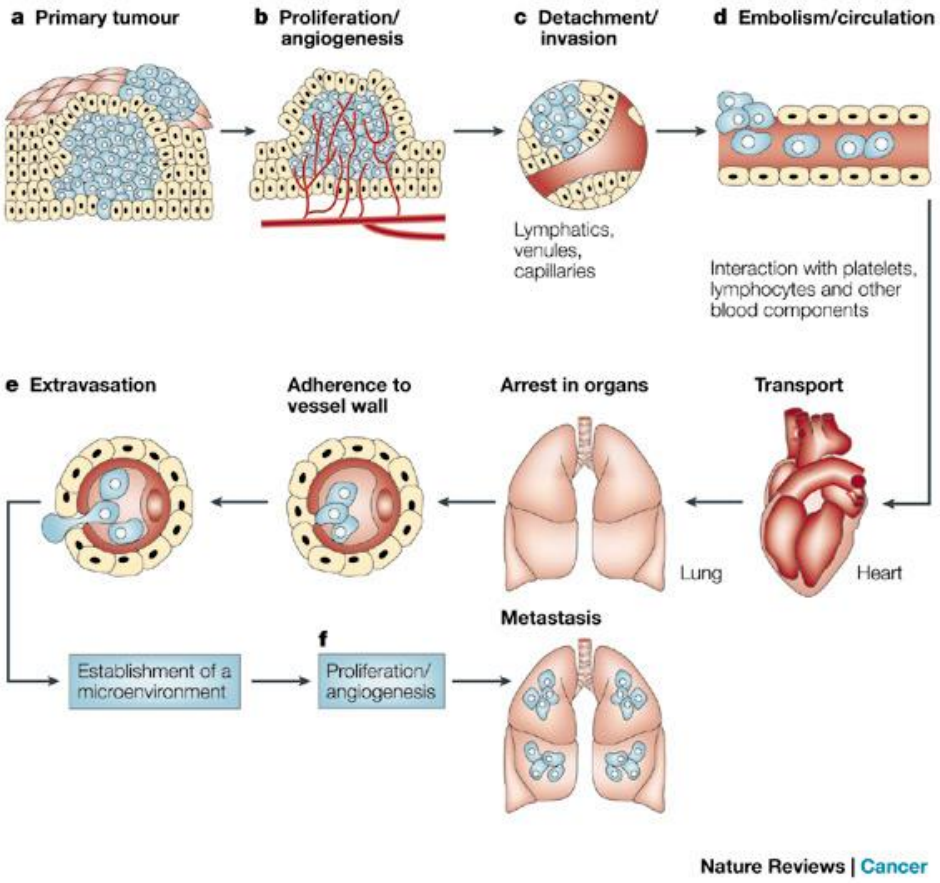

Figure 1-1 (a) Cellular transformation and tumor growth (b) formation of new blood vessels to the tumor sites (c) cancer invasion (d) circulation of tumor cells and reaching to distance sites (e) tumor cells leave the vessels to find new host, and (f) proliferation within the new host and formation of new vascular networks to the tumor sites. This cycle might be repeated. Reprinted by permission from Macmillan Publishers Ltd [2].

In order to clinically treat cancer, it is important to develop novel anti-metastasis drugs that can prevent the spread of cancer. These candidate drugs can be developed upon our understanding of metastasis mechanism at the very early stage which includes cell migration and invasion of cancer cells through the surrounding ECM. Unfortunately, monitoring the effect of the candidate drugs on inhibiting the cell invasion and angiogenesis is challenging.

Cell invasion and migration have many similarities. Cell migration is prerequisite of cell invasion. In cell migration, ECM is the substrate carrier for cell adhesion and movement. In the process of cell migration, cells polarize and elongate a leading edge toward the migration direction. This tail then apply a traction force on the cell body which produce a gradual cellular movement

on the ECM [3]. In cell invasion, cells advance through the ECM which acts as a barrier. Therefore, this process involves degradation or remodeling of ECM to facilitate the cell passage [4].

1.2 *In vitro* transmigration-invasion assays

Traditionally, 2-D culture systems were widely used to study the interaction of cells with each other and biochemical reagents in culture plates, culture flasks, and Petri dishes due to ease of use and high viability of cells on 2-D surfaces [5, 6]. However, cells behave on 2-D and 3-D surfaces in many different ways. 3-D scaffolds are more suitable for cells to interact with neighboring cells and ECM in a natural way. 3-D scaffolds can be engineered to contain the same proteins as the native tissues. Their mechanical properties can be tuned to help cells organize themselves and communicate with each other. The role of focal adhesion in cell motility is completely different in 2-D and 3-D systems [7], and cell migration and invasion is a process bounded to a 3-D environment. In this regard, hydrogels have been being used extensively as scaffolds to model ECM as they are water abundant, biocompatible, and their physical and chemical characteristics can be adjusted to create a biologically relevant microenvironment.

The traditional *in vitro* models developed first by Boyden to study transmigration and invasion assays in 2-D typically encompasses a cell culture insert housed inside a culture plate as shown in Figure 1-2. The insert consists of a porous membrane with a predefined size depending on the size of cells to be monitored. Cells are cultured on the insert and the media with chemoattractant of interest (eg, cell media + candidate drug) is added to the culture plate below. The cell migration is characterized by the number of cells passing through the porous membrane. Furthermore, cell invasion assay can be performed by coating a layer of ECM proteins on top of the insert. Such platforms have been developed to classify the invasion rate of lung cancer cells [8], study migration of single tumor cells [9], study the effect of specific proteins on the migration of brain cancer cells [10]. Additionally, similar platforms have been developed to

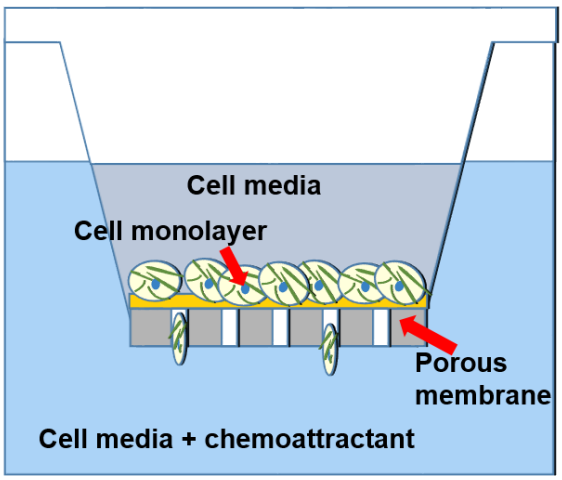

Figure 1-2 Boyden chamber consistsing insert and cell culture plate. Cells are seeded on the porous membrane separating the two.

increase and diversify the functionalities of this commercial products. For instance, wound healing assay is utilized to measure the rate of cells can repair a damaged wound [11, 12]. Spheroid migration assay [13, 14] is used to monitor the migration behavior of tumor spheroid clusters on a 2-D surfaces and etc. *In vitro* trans-migration and invasion assays enable the examination of a particular candidate drugs on the cells of interest without the presence of other proteins and cells. These assays are inexpensive, and can be performed easily, in a short period of time and is suitable for high throughput screening. Furthermore, this type of *in vitro* testing can be used to test the validity of some certain drugs prior to animal testing to reduce the quantity of animal suffrages which has raised many ethical questions. However, these platforms are primitive and do not have the complexity of *in vivo* microenvironments in terms of structures, functionalities and fluidic circulations.

With the help of microfabrication techniques and utilizing microfluidics, researchers have been able to extend the applications and complexity of the commercial *in vitro* migration and invasion assays. A microfluidic platform is developed to study the cell invasion of endothelial and cancer cells [15, 16]. As shown in Figure 1-3, this platform consists of two side channels and one central channel which are connected to each other by collagen hydrogel scaffold. Cells are introduced to the central channel and the control and chemoattractant media are introduced to the side channels. This platform enables to study the migratory phenotype of different types of cells by changing the biochemical cues. A multi-layer microfluidic device is developed to model vascular/valvular three-dimensional environment [17]. As shown in Figure 1-4, this platforms consists of two overlaying channels separated by a porous membrane. The bottom channel is filled with gelatin methacrylate (gel-MA) co-cultured with valvular interstitial cells (VICs), the top channel provides fluidic access, and the membrane is cultured with vascular endothelial cells. This platform was applied to investigate shear stress-regulated paracrine interactions between valvular endothelial cells and valvular interstitial cells. Several other microfluidic-based prototypes are developed with various functionalities and applications; analyze the specificity of human breast cancer cells to bones in a microenvironment that similar to vascularized osteo-cell microenvironment [18], study the breast cancer progression from early stage non-invasive ductal carcinoma *in situ* (DCIS) to the late stage invasive ductal carcinoma (IDC) [19], study the cell invasion characteristics of breast cancer cells (MCF7) by generating epidermal growth factor (EGF) concentration gradient across the cell

channel and suppressing their invasion by an anti-invasion, matrix metalloproteinase inhibitor GM6001 [20], quantify the migration and extravasation phenotype of primary tumor cells such as HepG2, HeLa, and MDA-MB 435S through a series of narrow capillary micro-channels [21]. These platforms mimic the physiological conditions cells undergo in *in vivo* microenvironments by integration of biochemical and biomechanical factors. These conditions permit the study of biological processes such as cell invasion *in vitro*, however lack the cell architecture found within the tissues and organs [22-26].

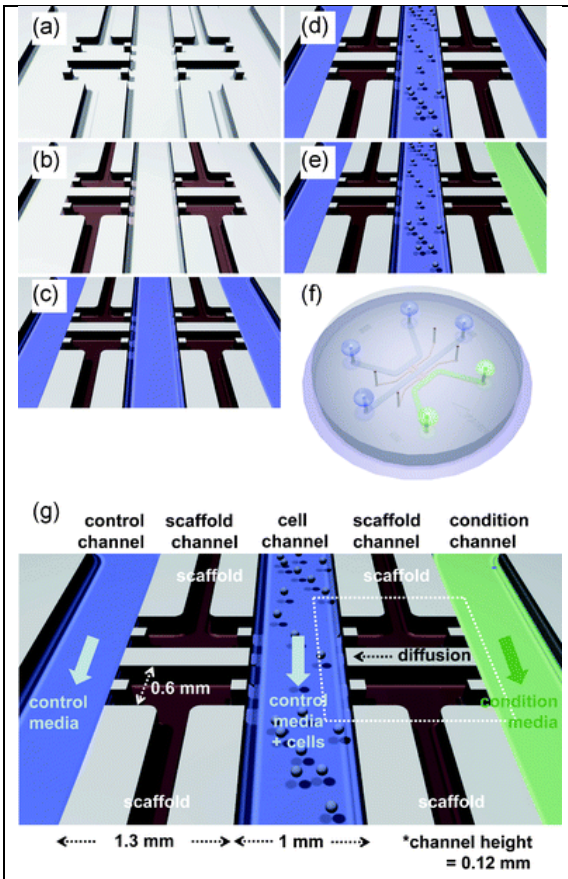

Figure 1-3 (a) Multichannel PDMS device, (b) filled gel scaffold in the scaffold channel between the channels, (c) media filling both channels, (d) cell seeding in the central cell channel, (e) chemical factors applied in the condition channel. (f) microfluidic device after filling of medium and chemical factors, (g) Schematic for microfluidic cell migration assay enabling direct comparison of cell migration behavior between the condition and control sides. Reproduced from [15] with permission of The Royal Society of Chemistry.

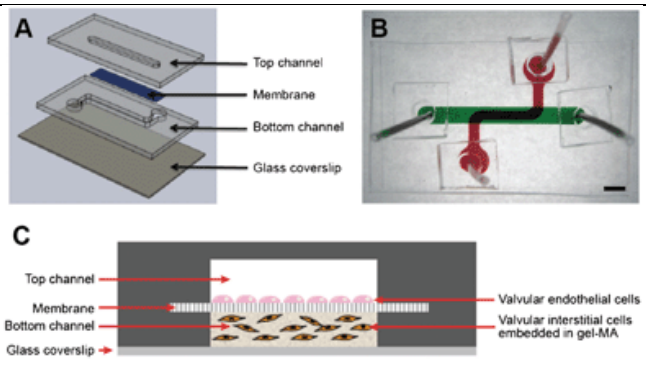

Figure 1-4 (a) Schematic and (b) photograph of bilayer membrane microfluidic device. The scale bar in panel (b) is 5 mm. (c) Cross-sectional schematic illustrating the spatial arrangement of the cells in the device. Reproduced from [17] with permission of The Royal Society of Chemistry.

1.3 Organ on chip

Researchers are further paving the path by combining microfabrication, microfluidics, and biology towards building *in vitro* microenvironments that can reconstitute the tissue architecture and functional complexity of living organs [27]. Although many of these devices are cultured with limited number of cell types, the mechanical function of the chips such as cyclic peristaltic motion, shear fluid flow, and blood flow rate emulates physiological conditions present in the respective organs. Such micro-devices are more complex in terms of **structure**, **functionality**, and **fluidic circulation** than previously described *in vitro* micro-devices. Such devices can be utilized to perform studies that conventional 2-D and 3-D cell cultural systems might not be able to recapitulate [28, 29]. As shown in Figure 1-5, these devices may mimic the tissue architecture and functionality of organs such as lung [30, 31], liver [32, 33], intestine [34], kidney [35, 36], vascular system [37, 38] and etc.

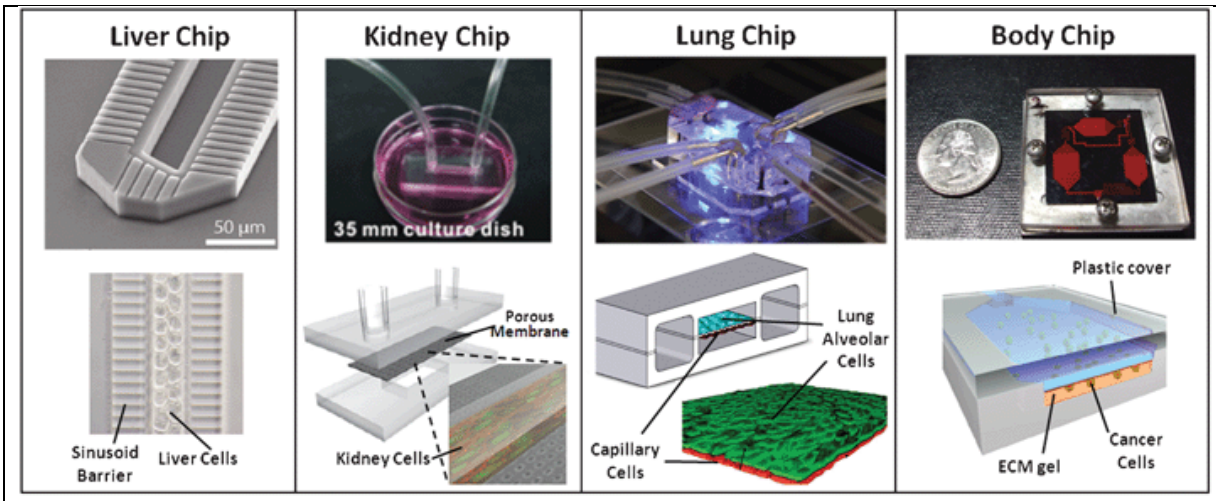

Figure 1-5 Mimicking tissue–tissue and organ–organ interfaces in organomimetic microdevices. Reproduced from [27] with permission of The Royal Society of Chemistry.

For instance, an *in vitro* microvascular networks as shown in Figure 1-6 developed by lithographic patterns of vessels in collagen hydrogel for further study in the field of cardiovascular biology [37]. The capabilities of this endothelialized cardiovascular network was demonstrated mainly by evaluating the stability of these vessels under perfused media and co-cultured cells, transforming nonthrombotic to thrombotic status of these vessels with treating endothelial cells and experimental verification during an inflammatory response. This system consists of multiple networks with junctions in 3-D collagen matrix which can go through angiogenesis re-modeling with the collagen concentration mimics the tissue stiffness surrounding the blood vessels. Therefore, such platform enables more complex studies of biological processes such as cell invasion and migration by recapitulating the architecture of blood vessels.

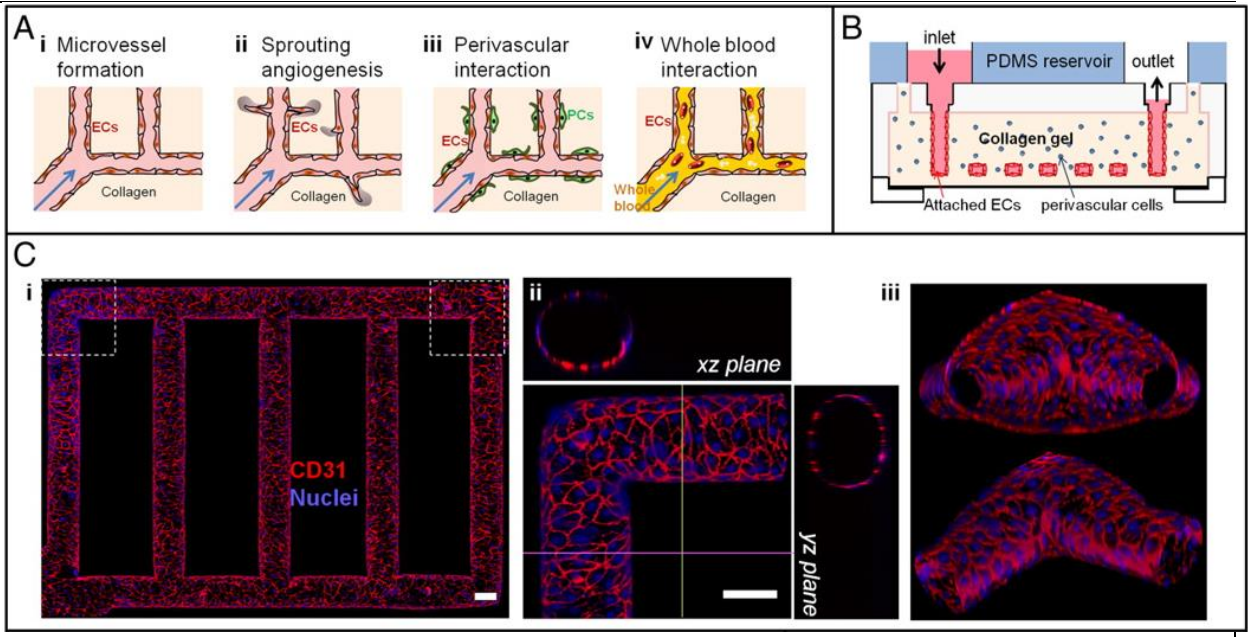

Figure 1-6 Microfluidic vessel networks (μVNs). (a) Schematic cross-sectional view of a section of μVN illustrating (*i*) morphology and barrier function of endothelium, (*ii*) endothelial sprouting, (*iii*) perivascular association, and (*iv*) blood perfusion. Arrow, Flow direction. (b) Schematic diagram of microfluidic collagen scaffolds after fabrication. (c) Z-stack projection of horizontal confocal sections of endothelialized microfluidic vessels (overall network, *i*) and views of corner (*ii*) and branching sections (*iii*). Red, CD31; blue, nuclei. scale bar: 100μm. Reproduced from [37] copyright 2012 National Academy of Sciences, USA.

The development of 3-D multi-cellular co-culture systems which simulate aspects of the *in vivo* microenvironment has led to biological insights in the role of the host environment in tumor biology. This has also resulted into a new generation of drug screening platforms that hold promise for discovery of anti-cancer agents better able to rid patients of tumor cells lodged within tissue [22, 39-41]. However, the fabrication of rapid throughput tissue mimetic 3-D cultures for cancer invasion assays has lagged particularly in light of its clinical significance [22, 26, 42, 43] for it is widely accepted that early management of invasive tumor cells could markedly blunt the impact of this disease.

1.4 Research contribution

The overall goal of this research lies on creating an *in vitro* microenvironment that mimics the features found in native tissues and studying the cell-ECM interaction on the interface of MEMS-Biology-Chemistry (Figure 1-7). This research work has contributed to the development of new techniques to develop bio-inspired geometries and enhances our understanding of interaction between biology and such microenvironments. In brief, we have achieved the following: (1) We have created a robust and reliable fabrication technique to create complex structures in a wide variety of bio-compatible materials such as polydimethylsiloxane (PDMS) and collagen hydrogel. This technique enables the fabrication of semi-circular features with ability to change the width and depth in one single etching process. Such features represent many native tissue structures such as blood vessels. Furthermore, this work has been spun off to develop 3-D structures in PDMS for bioelectrical characterization and separation of cells. (2) We have investigated the interwoven effect of chemical and mechanical (structural) cues on cell sprouting. The major goal of this study is to investigate the effect of the

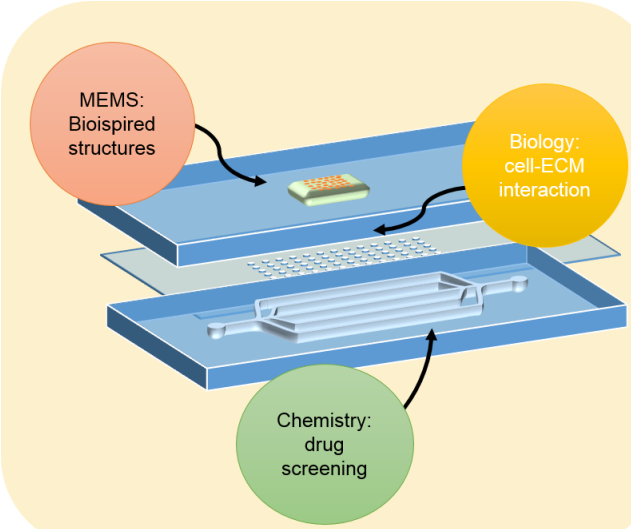

Figure 1-7 overall contribution toward creating a 3-D microenvironment for *in vitro* toxicology assays.

substrate microscale topographies on endothelial cell (EC) migration and capillary formation. Exploring cell-ECM interactions have the potential to elucidate understanding of these basic mechanisms will provide novel designs for vascular-targeting cancer treatments, and potentially improve the performance of existing anti-vascular drugs which have been a major research and investment focus, despite their relatively poor performance in the clinic.

Chapter 2. A Single-Mask Process for 3-D Microstructure Fabrication in PDMS

This chapter is reprinted from [44] with permission from IEEE MEMS Journal
Y. Hosseini, P. Zellner, and M. Agah, "A Single-Mask Process for 3-D Microstructure Fabrication in PDMS," *Journal of Microelectromechanical Systems*, vol. 22, pp. 356–62, 2013.

2.1 Introduction

Elastomers such as PDMS are widely used for lab-on-a-chip applications as they are transparent, bio-compatible, and low cost. Researchers have mainly utilized polymeric substances to develop 2-D microfluidic structures due to the simplicity of the fabrication process. For many research groups, soft-lithography [45] has still remained a popular option for developing structures in elastomers due to its cost effectiveness. In this technique, the negative features of the desired patterns in 2-D is transferred to a master device (*e.g.*, SU-8) once at a time using lithography techniques. Therefore, fabricating structures with different depths requires laborious and time-consuming multiple steps of lithography. Furthermore, this technique only enables the fabrication of sharp geometries (*e.g.*, rectangular channels), a limitation set by the lithography process and pattern transfer from the photomask to SU-8 resist.

However, realizing a comprehensive micro electro-mechanical system (MEMS) device with complex functionalities requires the development of 3-D geometries in a time and resource effective manner. For instance, biologically-inspired structures such as blood vessels or respiratory systems have much more complex shape than simple rectangular microfluidic channels that can be developed utilizing basic lithographic techniques to simulate such environments. For example, in blood vessels, cells are interacting inside circular channels, with varying diameter along with multiple branching and joints, with each other and their surrounding environment. Thereby, only under such condition one can truly study the biology of cells within a system *in vitro* as it is occurring *in vivo* if the microfluidic device resembles the structures of their living conditions [46].

There have been different approaches taken to facilitate the fabrication of 3-D complex structures throughout the past decades. In gray-scale lithography, masks with optical gradient contrast, unlike binary masks, have been utilized to fabricate structures with varying step profile with a single exposure [47, 48]. In direct deposition process, the scaffold of microstructures are

patterned serially by a robotic arm and infiltrated by photocurable materials. This is followed by the extraction of the scaffold to fabricate complicated networks of microfluidic channels [49]. In multi-photon absorption technique, a high energy beam is focused onto polymer resists causing the formation of highly cross-linked solid polymers which are stacked on top of each other forming a 3-D structure [50, 51]. In addition, there have been a few efforts on the fabrication of circular microfluidic channels [52-54]. Fiddes *et al* [53] reports the development of 3-D circular channels by first filling a regular 2-D rectangular channel with silicone oligomer solution and then introducing a coaxial stream of gas to form the circular-shaped channels along the gas stream. Furthermore, Song *et al* [54] demonstrates the fabrication of such channels by embedding a thin wire inside the mixture of PDMS pre-polymers before polymerization and removing the wire after polymerization.

The current methods require complicated and processes and tools in order to fabricate 3-D structures. Some of these techniques lack the possibility of fabricating circular channels in a robust manner [47, 48, 50, 51] and techniques developed for the fabrication of 3-D channels are not suited for fabricating circular channels with constantly varying dimensions [49, 52-54]. These limitations have encouraged our group to research and establish a reliable and robust yet low cost technique for the fabrication of versatile 3-D structures in PDMS.

This paper describes in details the fabrication processes of such 3-D structures in PDMS based on our previous research on fabricating 3-D structures in silicon, transfer of the negative replica of silicon to glass, and eventually the transfer of original patterns in silicon to PDMS utilizing the soft-lithography technique using the glass structure. In addition, as a case example, this paper demonstrates the applicability of this technique in realizing the first polymeric 3-D insulator-based dielectrophoresis device that can be used to trap and enrich biological particles. The following sections discuss in details the fabrication methods utilized to achieve such 3-D structures in silicon and consequently in PDMS.

2.2 3-D fabrication process

RIE lag or Aspect Ratio Dependent Etching (ARDE) assists to create large features by etching multiple smaller features [55, 56]. We have previously reported on the fabrication of 3-D microfluidic structures in silicon with a single-mask process taking advantage of the RIE lag

effects [57, 58]. In this technique, a single mask with five independent geometric variables similar to those shown in the prior work [58] along with the etch time can determine the depth and width of the microfabricated channels. The method allows the realization of complex symmetric and non-symmetric microfluidic channels and cavities by isotropic etching of silicon in sulfur hexafluoride (SF_6) plasma using reactive ion etching (RIE) technique.

More specifically, the fabrication procedure starts by depositing 3000Å of silicon dioxide on a silicon wafer. The oxide is deposited with a PECVD (Trion Orion II, USA) at 300°C. In the next step, photoresist is spun and patterned with many micron-scale windows (Figure 2-1a–b). This window pattern enhances the RIE lag effect, allowing for large differences in depth to be achieved. The oxide layer is patterned according to the photomask. Then, silicon is etched in an DRIE (Alcatel, AMS-100, France). During the silicon etching process, the patterned oxide lattice structure remains suspended above the microchannel. The local rate of the silicon isotropic etching process is dependent on the window pattern. As a result, a 3-D topography is formed by using different patterns on the photomask. As previously reported [58], the depth and width of the microchannel is related to the independent geometric values and etch time by equation (2-1)

$$\text{Depth} = \exp\left(\frac{\alpha\beta F^{\gamma}}{1+\beta F^{\gamma}}\right) \tag{2-1}$$

In this equation, α, β, and γ are a function of the etch time t and the window pattern factors c, w, l, and s. c is the number of windows in a row, s is the window spacing, w is the width of a window, and l is the length of a window. The fill factor F is given by equation (2-2)

$$F = c\left(\frac{wl}{(w+s)(w+l)}\right) \tag{2-2}$$

By changing the geometrical patterns, different channels with varying depths and widths can be fabricated and their dimensions can be predicted by the aforementioned models. Using such scheme, it was shown that for channels with small width (less than 30μm), it is possible to obtain a nearly semi-circular (aspect ratio 1:1) shape, whereas increasing the channel width will decrease the aspect ratio. For very wide channels (larger than 300μm), it is possible to obtain a rectangular cross section with nearly rounded corners. In addition, the depth profile of the transition between two different depths can be controlled by creating gradients of different window parameters.

Figure 2-2 shows to some extend the complexity of 3-D structures and quality of surfaces fabricated in silicon utilizing RIE lag using this technique.

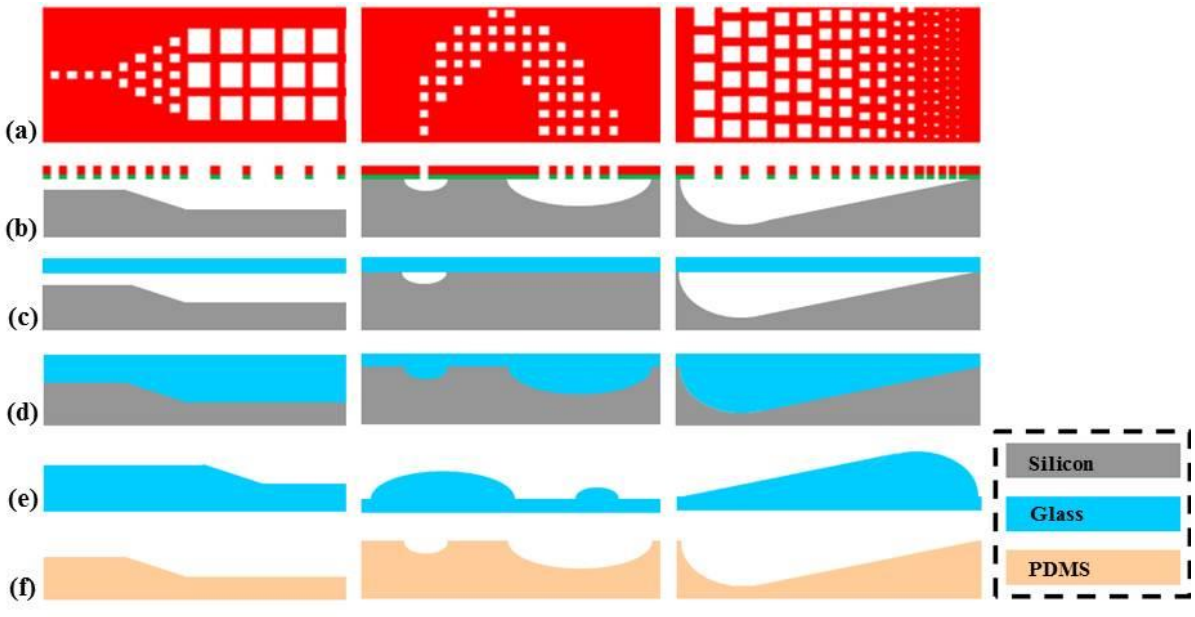

Figure 2-1 Process flow of fabrication of 3-D structures in glass and elastomers. (a) photomask layout to induce RIE lag (b) silicon isotropic RIE SF_6 plasma etching, (c) anodic-bonding of silicon and glass in vacuum, (d) glass reflow, (e) silicon etch to release the glass device, and (f) pouring PDMS prepolymer, curing, and peeling PDMS replica from the glass master.

After the fabrication of the 3-D silicon device, the negative replica of silicon in glass and the positive replica of silicon in PDMS are fabricated employing the following procedures. First, both the surface of the silicon wafer comprising 3-D structures and a blank 700µm-thick Borofloat® 33 wafer are immersed in NanoStrip (Cyantek, CA, USA) for 20 minutes to remove any organic residues from the surface of the wafers. Then, silicon and Borofloat wafers are anodic-bonded under vacuum employing a substrate bonder (Karl-Suss, SB6, Germany) (Figure 2-1c). The bonded structure is placed in a high temperature oven and its temperature is elevated and maintained at 720°C for about 4 hours and then is gradually increased to 760°C with 10°C min^{-1}. The structure is kept at this temperature for 30 minutes. Under these conditions, glass reflows and fills the channels and cavities formed in silicon (Figure 2-1d). After cooling down the melted device, the surfaces of the bonded wafers are cleaned by immersing them in a 10:1 buffered Hydrofluoric acid (BOE) to remove any oxide growth on silicon during the reflow process.

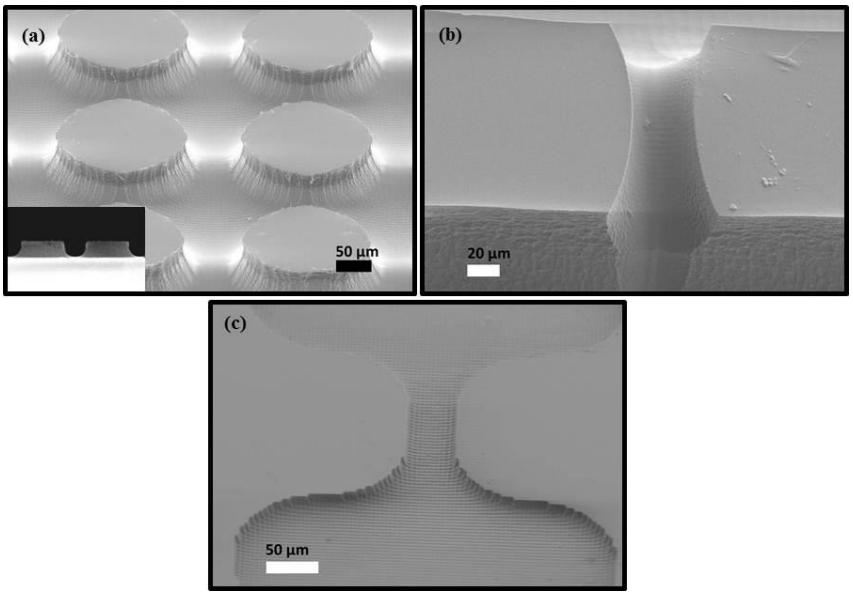

Figure 2-2 3-D structures fabricated in silicon utilizing RIE lag. These structures comprising more complex structures that contain channels with different width and depth, depth transition, and other geometries that might not be simple to achieve utilizing multiple steps of 2-D lithography (a) microposts for use in insulator-based dielectrophoresis as well as CTC trapping with the inset showing the cross-section view, (b) 40µm-deep channel connecting two 100µm-deep channels together, (c) a flow-cytometry chamber, 40µm-deep in the narrow section and 90µm-deep in the deeper section.

Subsequently, the silicon substrate is completely etched by Potassium hydroxide (KOH) at 95^{o}C leaving behind the glass microstructure device having the negative replica of the silicon structures (Figure 2-1e). In order to obtain the positive replica of the 3-D structures in PDMS, the surface of the glass master is silanized by vaporizing a couple of droplets of trichloro(1*H*,1*H*,2*H*,2*H*-perfluorooctyl)silane (Sigma-Aldrich, MO, USA) for 2 hours inside a desiccator to ensure smooth and safe release of the PDMS mold. Then the pre-polymer and curing agent of Sylgard 184 (Dow Corning, MI, USA) are mixed for the ratio of 10:1 and poured gently on the surface of the glass master. The device is again placed inside a desiccator and PDMS is degassed for about 1 hour. The glass master along with the uncured PDMS device is then placed in an oven at 100°C for one hour. The PDMS structure is then separated from the glass master while replicating the same 3-D features on the original silicon substrate (Figure 2-1f). As evident, due to isotropic etching at the beginning of the process, sharp corners and edges in the final PDSM structures are avoided.

2.3 Results and discussion

I. Glass reflow factors

In order to replicate the 3-D features of silicon to PDMS, while heated in furnace, glass should reflow into the cavities of silicon and fill them completely. To achieve this, the reflow temperature and duration should be properly set. In an ideal case, it is desired to ramp the furnace temperature to the softening point of Borofloat wafer (820°C) for enough time to ensure that the glass wafer reflows and fills the cavities etched in silicon. However, as the temperature of the furnace is being increased, small bubbles start to form on the surface of the glass wafers, which at some cases can occur inside the silicon cavities, hence deforming the final shapes and geometries in glass. The presence of such bubbles on the surface of glass wafers can be attributed to the re-boiling effect, which usually occurs at high temperatures on the junction of non-well controlled surfaces (in this case, the anodic-bonded surface of glass and silicon) [15]. Bubbles appear on the surface of glass structure where it faces the silicon wafer. In this work, attempts have been taken to avoid the presence of such detrimental effects as much as possible. Figure 2-3 shows the surface images of glass wafers after being heated at 800°C for 20 minutes and 760°C for 8 hours. The glass wafers were bonded to blank silicon wafers prior to placing in the furnace and the silicon wafers were removed after the glass reflow procedure. Furthermore, Figure 2-4 shows the SEM images of the surface of the glass wafer, which contain some structures, after the reflow process at 760°C for 8 hours. These defects, if untreated, will be transferred to the PDMS mold, and leave additional small and round pieces of PDMS atop the mold on the spots of the defects.

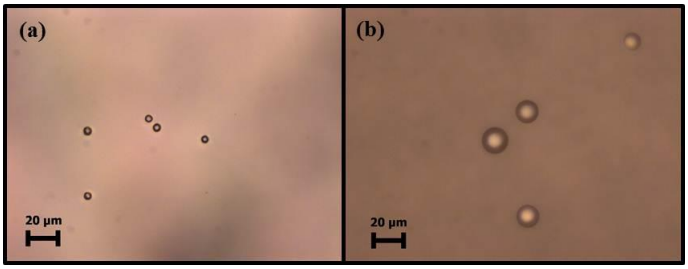

Figure 2-3 (a) Glass surface after heat treatment at 760°C for 8 hours and (b) glass surface after heat treatment at 800°C for 20 minutes. Reboiling effect has caused the formation of small bubbles on the surface of both wafers.

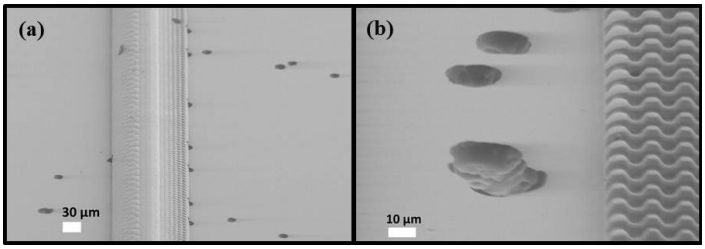

Figure 2-4 SEM images of glass structure after heat treatment at 760°C for 8 hours and silicon removal (a) Glass master device with bubbles spread around and (b) close-up view of bubbles on the surface of glass master.

In order to alleviate the re-boiling effect, we adjusted three factors including temperature ramp rate, reflow temperature, and reflow time. The furnace temperature was ramped to the target point gradually (10°C min^{-1}). As illustrated in Figure 2-3 and Figure 2-4, this factor solely cannot help to eliminate the defects on the surface of glass but sudden increase of the furnace temperature will result in the formation of much more bubbles. Furthermore, the furnace temperature was reduced to below the softening point of Borofloat for a various range of time. Then, the furnace temperature and the reflow time were recorded. Table 2-1 reports the conditions which resulted in a bubble-free glass surface with a check-mark (✓) and those which resulted in the formation of bubbles on the surface of the glass with a cross-mark (×). In order to both obtain a bubble-free glass structure and ensure complete reflow of glass in the silicon cavities, it was chosen to first maintain the furnace temperature at 720°C for 4 hours and then ramp the furnace temperature to 760°C for 30 minutes. As Figure 2-5 shows, glass has completely filled the silicon cavity using the above temperature and time settings.

Table 2-1 Reflow temperature and time effect on the formation of bubbles on the surface of glass

Time / Temperature	20 MINUTES	40 MINUTES	8 HOURS
700°C	✓	✓	✓
720°C	✓	✓	✓
750°C	✓	✓	×
770°C	✓	✓	×
800°C	×	×	×

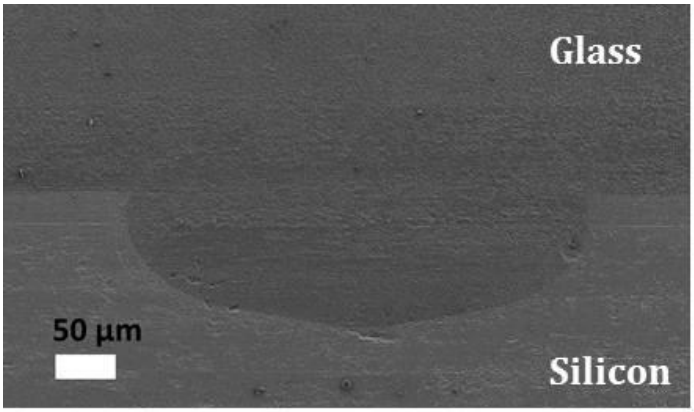

Figure 2-5 Bonded surface of glass and silicon after reflow process. The device was placed in a furnace at 720°C for 4 hours and then at 760°C for 30 minutes.

II. 3-D pattern transfer from silicon to glass and PDMS

Figure 2-6 shows images of several glass microstructures after they are released from silicon, clearly depicting out-of-plane structures with different heights and widths. Figure 2-7 shows the images of several PDMS prototypes fabricated using the glass structures as master. As the glass wafer fills the silicon cavities after the reflow process, all the features of the original structures are transferred to the PDMS mold. The surface of the PDMS mold is, however, very smooth on the area that the glass wafer was faced the un-etched area of the silicon wafer. These complex 3-D devices can find numerous applications including microfluidic mixing, cell and particle separation and enrichment, and droplet splitting. The ability to create both constant depth and variable depth channels increases the design flexibility of all of these devices. The structure in Figure 2-7a is a capillary network with channel depths ranging from 10µm to 80µm which can be used to simulate blood vessels in the human body. Similar types of structure have been fabricated by melting photoresist to form the master structures [59, 60], however, this method requires additional steps of lithography to enable controlling the width and depth of the channels simultaneously. Figure 2-7b shows a microchannel composed of 400µm-wide, 20µm-deep chambers which are connected by smaller channels measuring 7µm in both depth and width. This structure may be used for flow cytometry to observe a single particle at a time. Using this 3-D architecture, particles from a large main channel can be brought into a small focus channel where they are positioned in width and depth for imaging. Figure 2-7c shows a spiral which varies smoothly in depth from 25µm to 50µm

and in width from 25μm to 100μm. In Figure 2-7d, two 50μm deep main channels are separated by a series of smaller channels which are 15μm-deep and 20μm-wide. This structure may be used to study cell migration through narrow passageways.

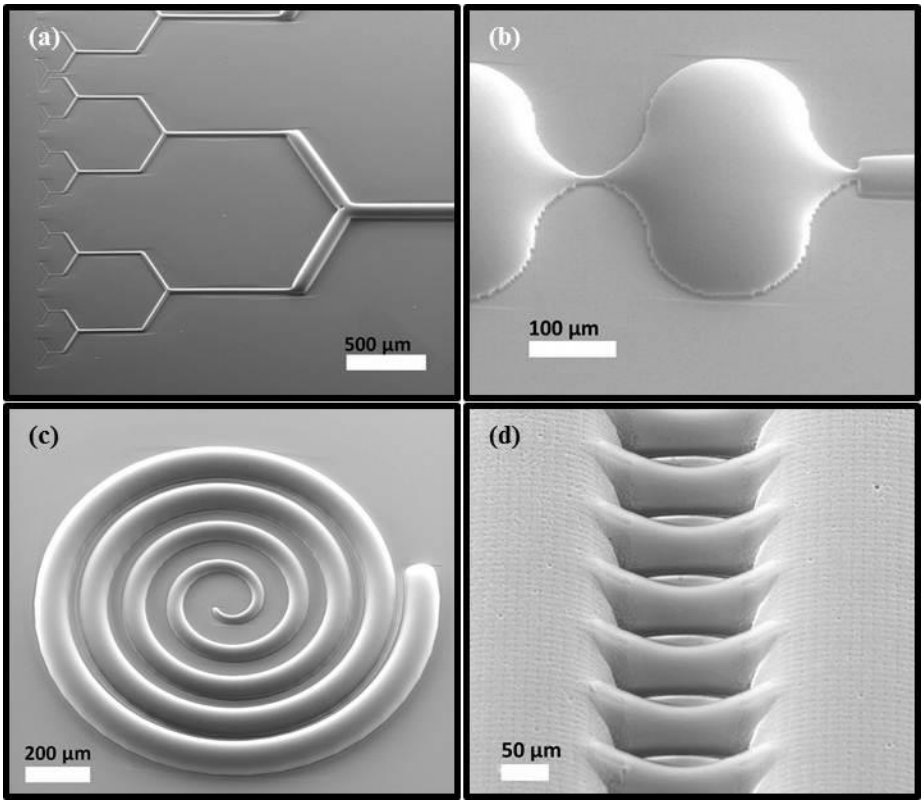

Figure 2-6 SEM images of several glass device prototypes after silicon release. The glass structures include replica of channels/cavities with different height and width.(a) capillary network, (b) micro-flow cytometry chamber, (c) spiral, and (d) cell migration passageways. Scale bar represents the actual dimension only in lateral-direction as the images are tilted in vertical-direction.

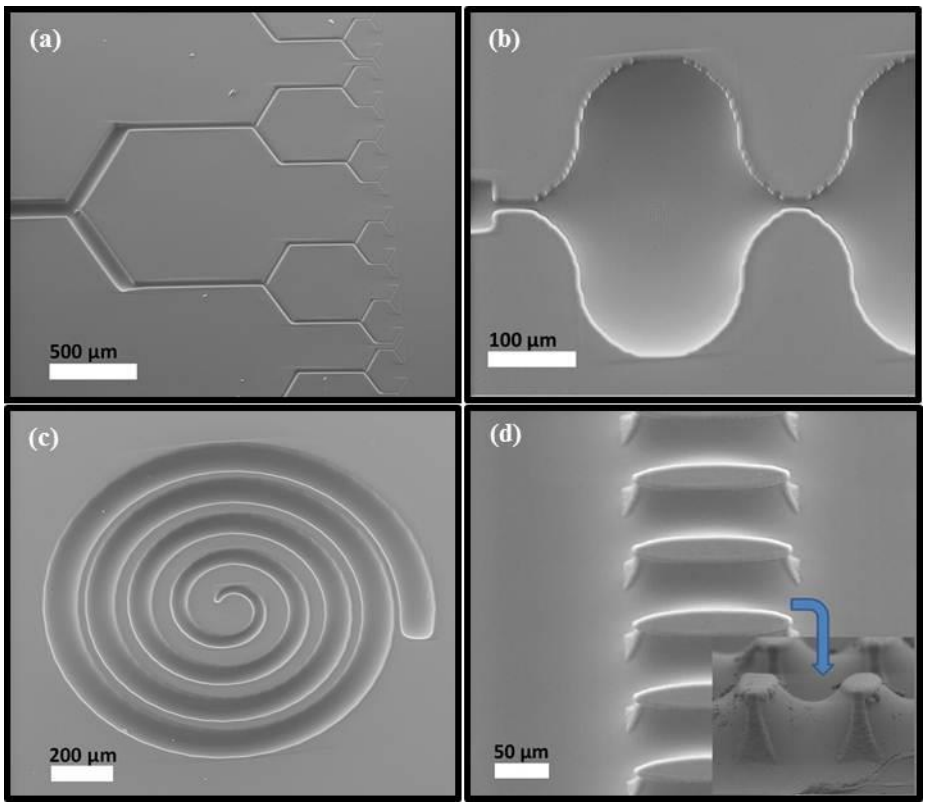

Figure 2-7 SEM images of several 3-D microfluidic devices made in PDMS using the master structures depicted in Figure 6. (a) capillary network, (b) micro-flow cytometry chamber, (c) spiral, and (d) cell migration passageways with the inset showing 90^0 rotated image. Scale bar represents the actual dimension only in lateral-direction as the images are tilted in vertical-direction.

III. ***PDMS devices with 3-D properties***

In order to demonstrate the versatility of this 3-D fabrication process, 3-D insulator-based dielectrophoresis (iDEP) devices were created and tested. iDEP microfluidic devices have been used to trap and sort bacteria, viruses, cells, and beads. Dielectrophoresis is the motion of polarizable particles that are suspended in an electrolyte when subjected to a spatially nonuniform electric field [61]. The DEP force felt by a spherical particle suspended in a medium is given by equation (2-3)

$$F_{DEP} = 2\pi R^3 \varepsilon_m \,\mathrm{Re}\left[f_{CM}\right] \nabla \left|\mathbf{E}\right|^2 \tag{2-3}$$

where R is the radius of the particle, ε_m is the permittivity of the medium, **E** is the local electric field, and $\mathrm{Re}[f_{CM}]$ is the real part of the Clausius-Mossotti factor. Fluid flow in iDEP devices is generated by electrokinetic (EK) flow. For a particle to become trapped in these devices, the DEP

force must be larger than the EK force on the particle. Mathematically, this is [62] given by equation (2-4)

$$\frac{u_{DEP} \cdot u_{EK}}{u_{EK} \cdot u_{EK}} = \frac{\mu_{DEP}}{\mu_{EK}} \frac{\nabla(E \cdot E)}{E \cdot E} \cdot E > 1 \tag{2-4}$$

where $u_{DEP} = \mu_{DEP} \nabla(E \cdot E)$ and μ_{DEP} are the DEP velocity and mobility of the particle, respectively, and $u_{EK} = \mu_{EK} E$ and μ_{EK} are the EK velocity and mobility of the particle, respectively. The DEP force increases as the square of the electric field while the EK increase linearly with the electric field. Thus, as the electric field strength increases, the DEP forces become dominant. When the DEP overcomes the EK flow, the particle is trapped. In iDEP, insulating structures are used to create the required electric field gradient.

The 3-D iDEP device presented herein consists of a 1.2mm-wide, 90µm-deep main channel and a 70µm-wide, 30µm-deep trapping channel. The transition between the two channels is smooth. Typical iDEP devices contain constrictions in width to create the required non uniform electric field [63, 64]. However, recently it has been shown that 3-D geometries can enhance the performance of iDEP devices by decreasing the applied voltage required for operation [65, 66]. The 3-D fabrication enhances the performance of the devices by creating larger gradients over wider areas when compare to those obtained in fixed depth devices. The 3-D geometry allows for large cross-sectional area constrictions within a short space. These sharp constrictions create high electric field gradients which in turn lead to high DEP forces. Thus, a 3-D device is able to create stronger DEP forces than a 2-D device with the same footprint. This allows for operation at lower applied fields.

For our experimental setup, 0.5-µm and 2-µm diameter polystyrene beads were suspended in DI water with a measured conductivity of 760µS m^{-1}. The solution was flowed through the microfluidic device and voltage was applied along the length of the channel from the 1cm spaced reservoirs. Trapping of 2µm beads was obtained at 150V with over 90% of all particles trapped (Figure 2-8). The trapping was shown to be reversible with 100% of the trapped particles released when voltage was removed. Trapping of 0.5µm beads was obtained at 350V with over 85% of all particles trapped (Figure 2-9). The trapping was shown to be reversible for 90% of the particles while the remainder became fixed to the channel floor.

iDEP devices typically require applied voltages from 400V cm^{-1} to 1200V cm^{-1} [62, 67-70]. However, the 3-D slopes in our device allowed for trapping at 150V. Lowering the required applied voltage decreases the joule heating in the channel which can kill biological particles and can create unwanted thermal currents in the device. Additionally, lowering the operating voltage decreases the complexity and cost of the electronics needed to actuate the device. Thus, the performance of the iDEP devices is enhanced by our 3-D fabrication method.

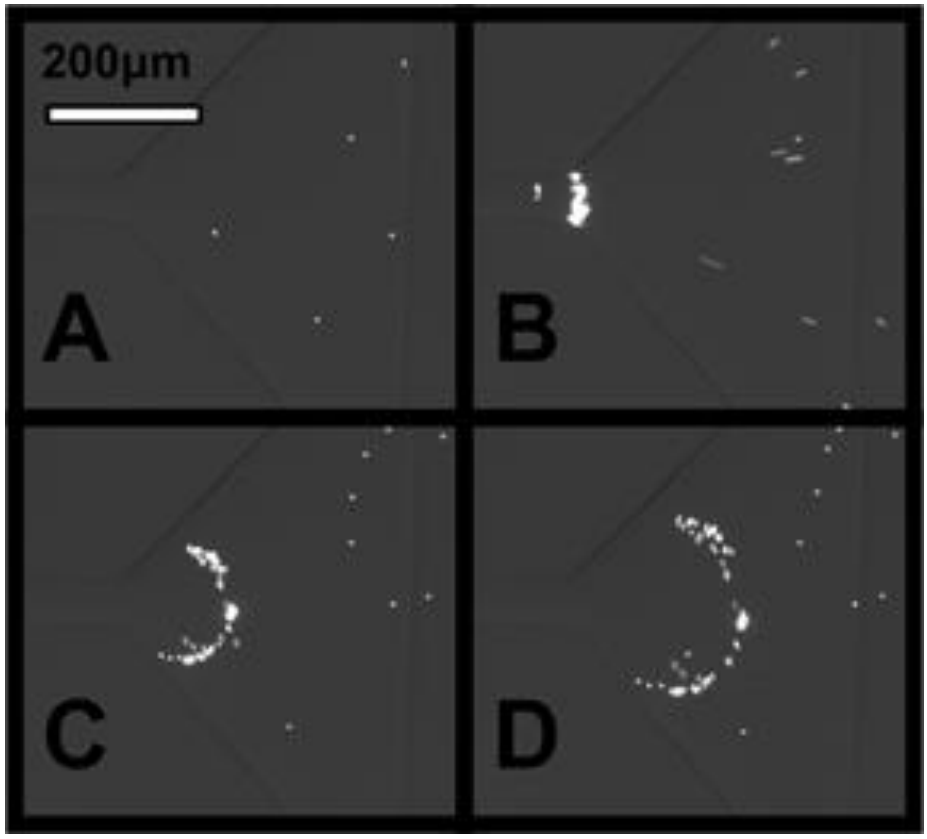

Figure 2-8 Trapping and release of 2-µm beads. (a) No voltage (b) 150V is applied (c and d) Voltage is turned off and particles are released.

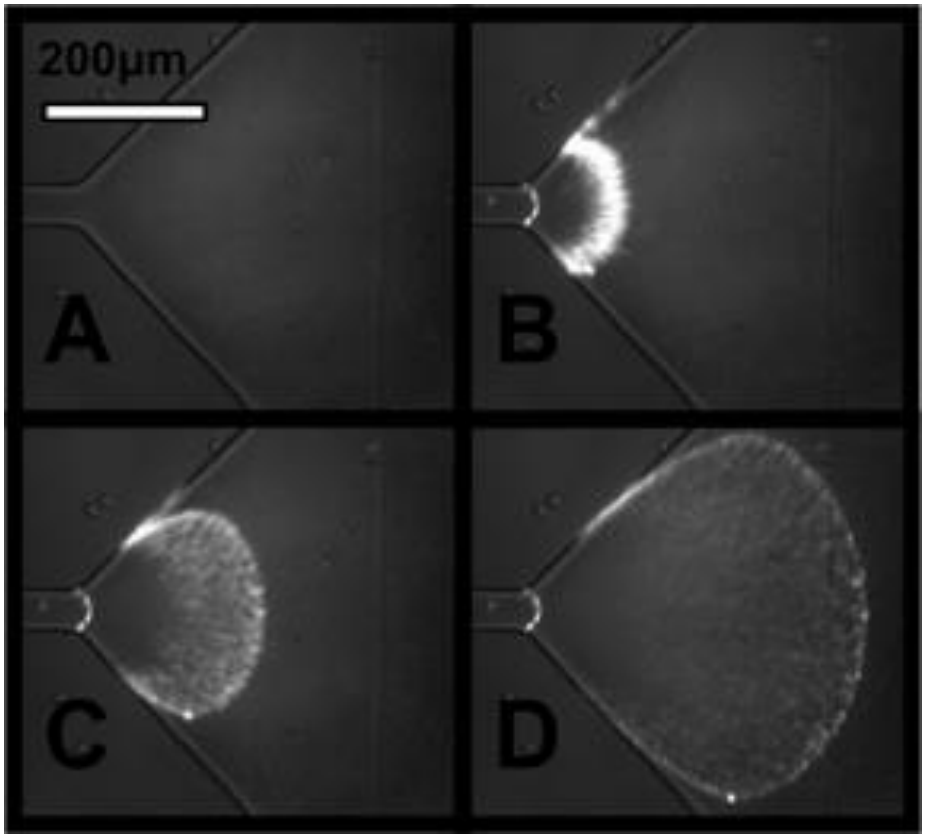

Figure 2-9 Trapping and release of 0.5-µm beads. (a) No voltage (b) 350V is applied (c and d) Voltage is turned off and particles are released.

2.4 Conclusion

The presented method provides a novel, low-cost, high-yield process to develop 3-D in-plane PDMS devices whose realization with other methods such as conventional multiple lithography and etching steps for forming the master is very difficult if not impossible. The width and depth of the structures can vary from a few hundred microns down to a few microns while transition between these changes can be controlled to be gradual. It is also notable that out-of-plane structures are formed in glass substrates in this technique. The main advantage of using the method described in this paper is the ease of the release of the glass master from the silicon structure. As the glass substrate contain out-of-plane structures, releasing the PDMS device is not difficult. If one wants to use an elastomer instead of glass and peel it off from the in-plane silicon substrate, the released structures are very likely to be damaged due to the undercut features present in the isotropically etched silicon structures.

Several microfluidic structures in PDMS have been demonstrated that can be used for cellular analysis, bioparticle enrichment, and bio-inspired network formation. In particular, 3-D structures were developed in PDMS for insulator-based dielectrophoresis. It was shown that these devices can operate at voltages which are at least a factor of 2 lower than voltages required to operate their 2-D counterparts. Enrichment of 500nm and 2μm were successfully demonstrated using applied voltages of 350V and 150V, respectively. The trapping efficiency was measured to be more than 80%. The high-performance 3-D iDEP can be used to enrich bacteria and other biological particles finding a variety of applications ranging from water and food safety to counter-terrorism.

Chapter 3. Bio-inspired Microstructures in Collagen Type I Hydrogel

This chapter is reprinted from [71] with permission from John Wiley and Sons
Y. Hosseini, S.S. Verbridge, and M. Agah, "Bio-inspired microstructures in collagen type I hydrogel," *Journal of Biomedical Materials Research*, vol. 103, pp. 2193–7, 2015.

3.1 Introduction

In tissue engineering, hydrogels are used extensively as scaffolds to model ECM as they are water abundant, biodegradable, biocompatible, and their physical and chemical characteristics can be adjusted to create a biologically relevant microenvironment [72]. Hydrogels can be synthesized chemically for instance with poly(ethyl glycol) (PEG) and poly(acrylic acid) (PAA), or extracted naturally from animal or plant tissues such as collagen, gelatin, alginate and chitosan [73]. Synthetic hydrogels are generally incorporated with additional peptides to increase the degree of the biocompatibility and biodegradability, and hence, suffer from some degree of toxicity. On the other hand, natural hydrogels consist of proteins similar to those found in the native tissue, which promote cell adhesion, migration, proliferation, and hydrogel degradation, and induce minimal antigenic response. In this regard, among the proteins that can be used to prepare natural hydrogels, collagen is widely utilized. Collagen accounts for 25–35% of all proteins in human body, of which 90% is type I collagen. Collagen I molecules, with the shape of triple helical segments, are assembled to form fibrils and cross-linked to form fibers [74, 75]. Collagen I can be easily extracted from animal tissues such as tendons of rat tails and calf skins.

Developing structures in hydrogel from collagen often requires molding neutralized collagen solution against a negative replica stamp before polymerization. Previous techniques typically rely on soft lithography to fabricate such stamps in PDMS to create fluidic channels and other simple structures, often in 2-D with sharp edges resulting from the nature of top-down patterning. Typically widths can be varied while depth remains fixed [37, 76-82]. Complex microvascular networks with rectangular cross-sections have been demonstrated [37, 78, 81], however, more biomimetic circular cross-sections, or devices with variable depths are not feasible with these lithographic techniques. Sacrificial techniques may provide rounded cross sections [78, 80], however, these methods are highly limited in the channel geometries that can be produced, and are

typically limited to single straight channels. Layered additive techniques such as 3-D printing approaches also generally suffer from poor resolution, with sub-100 μm features a challenge to fabricate using the extrusion methods [83].

In order to closely mimic the native tissue and tumor microenvironments, it is necessary to fabricate much more complex shapes and geometries. For instance, in blood vessels, cells are interacting inside circular channels, with varying diameter along with multiple branches and joints, with each other and their surrounding ECM environment. In this report, we have extended our previous work in 3-D tissue micropatterning [44, 58], working towards much more complex and physiologically relevant surface topographies in 3-D tissue utilizing a single mask, single etch process using reactive RIE lag.

3.2 Materials and methods

I. Collagen extraction

Collagen was extracted from the tendon of rat tail as previously detailed [84]. Rat tails were dissected under sterile conditions and their tendons were extracted and processed in 0.1% acetic acid at 4^{o}C for 48 hours. In order to remove the insoluble contents such as bits of fat and facia from the collagen solution, it was centrifuged (Avanti J-25, Beckman Coulter, CA, USA) at ×15,000g for 90 minutes. The solution was placed in a freezer overnight, and subsequently lyophilized for 48 hours until complete dryness, and then kept in the freezer.

II. Collagen hydrogel handling pre-crosslinking

Prior to experiments, collagen stock solutions at a concentration of 7.5mg ml^{-1} in 0.1% acetic acid were made. Collagen hydrogel at a final concentration of 5mg ml^{-1} was prepared from the stock solution. The following steps were carried out under sterile conditions: 1) in one microtube, the desired amount of collagen solution was added, 2) in another microtube, the dilutant media consisting of Dulbecco's Modification of Eagles Medium (DMEM) (Corning Cellgro, VA, USA) 10× (0.1 final volume neutralized collagen), NaOH (volume of collagen × 0.02), DMEM 1× (as much as necessary to adjust the final concentration) were pipetted and 3) the dilutant media was pipetted in the collagen solution and gently mixed with a small spatula to avoid the formation of bubbles. All tubes and mixing hardware were kept on ice to prevent premature cross-linking of the collagen. In order to facilitate the assembly of fiber molecules, the devices were placed inside a

sterile dish with a cover, preincubated at 4°C for 1 hour, and incubated at 37°C for 1 hour to cross-link the fibers.

III. ***Cells and culture media***

Human umbilical vein endothelial cells (HUVECs) (Lonza, MD, USA) were prepared and cultured in EGM2 basal media with a growth factor bullet kit (Lonza). HUVECs were used and patterned on 3-D microfabricated collagen chips between passages 3–7. 600 cells mm^{-2} were seeded on top of each collagen chip. After 48 hours, they formed a confluent monolayer on the hydrogel surface before fixation.

IV. ***Fixing and co-staining of fibers and cells***

Cells and collagen fibers were fixed at room temperature for 20 minutes with 10% buffered formalin phosphate (Fisher Scientific, NJ, USA). Between each step, the samples were washed 3 times with PBS for 5 minutes per rinse. Samples were permeabilized and blocked with 0.5% Triton-X 100 (Acros Organics, NJ, USA) in Superblock blocking buffer in PBS (Thermo Scientific, IL, USA) at room temperature for 2 hours. In the next step, they were incubated with primary mouse monoclonal anti-collagen I (Abcam, MA, USA) (1:1000) and rabbit monoclonal VE-Cadherin (Cell Signaling Technology, MA, USA) (1:250) at 4°C overnight, and incubated with Alexa Flour 546 anti-mouse secondary antibody (Life Technologies, NY, USA) (1:250) to stain the fibers, and with RedDot2 (Biotium, CA, USA) (1:200), Phalloidin 350 (Biotium) (1:250), and Alexa Flour 488 anti-rabbit secondary antibody (Life Technologies) (1:250), at room temperature for 1 hour, in order to stain the nuclei, actin filaments and cell-cell junctions, respectively.

V. ***Three-dimensional fabrication from silicon to collagen hydrogel***

The fabrication process flow from silicon to PDMS and hydrogel starts with etching the desired structures in silicon as explained previously [44, 85] as shown in Figure 3-1. In brief, a photomask parameter related to the geometrical value and etch time is generated based on the desired width and depth of structures as shown in equations (3-1) and (3-2)

$$\text{Depth} = \exp\left(\frac{\alpha\beta F^{\gamma}}{1+\beta F^{\gamma}}\right) \tag{3-1}$$

$$F = c\left(\frac{wl}{(w+s)(w+l)}\right) \tag{3-2}$$

In this equation, α, β, and γ are a function of the etch time t. The fill factor F is determined by equation (3-2). The window pattern factors c, w, l, and s. c is the number of windows in a row, s is the window spacing, w is the width of a window, and l is the length of a window [58]. These parameters are the size of openings and spacing in between that enables the fabrication of etched structures with 3-D structures across a single wafer utilizing reactive RIE (Figure 3-1a) (top view) and (Figure 3-1b) (cross-section view). In the next step, pre-polymer and curing agent for PDMS, Sylgard 184 (Dow Corning, MI, USA) were mixed in a 10:1 ratio, poured on the silicon structures, and thermally cured at 100^{o}C for 2 hours. In order to ensure the smooth release of PDMS from the silicon mold, the silicon surface was treated with trichloro(1*H*,1*H*,2*H*,2*H*-perfluorooctyl)silane (Sigma-Aldrich, MO, USA) (Figure 3-1c).

In order to fabricate the structures in collagen hydrogel, the PDMS stamp was briefly treated with oxygen plasma, and coated with 1% bovine serum albumin (BSA) to facilitate the release of the PDMS mold from collagen hydrogel. A pin was inserted on the backside of the PDMS mold and kept on ice until the mold was cast against collagen solution. Collagen hydrogel with a final concentration of 5mg ml^{-1} was made from concentrated collagen stock solutions of 7.5mg ml^{-1}, as

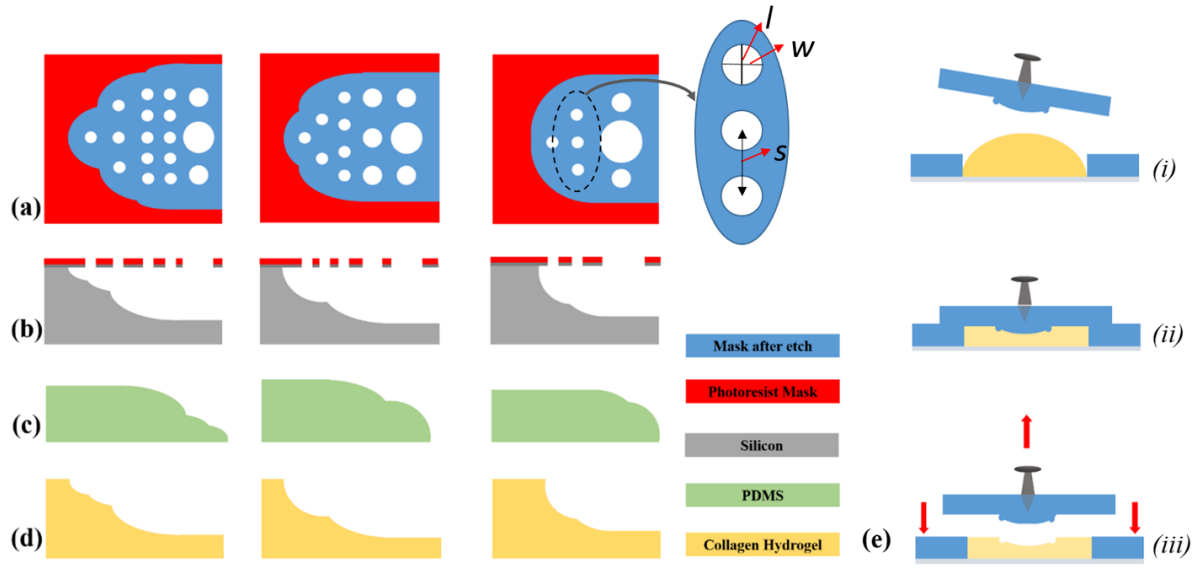

Figure 3-1 Fabrication process flow of 3-D pattern transfer from silicon to collagen hydrogel. (a) top view design of photomask; opening size and spacing controls RIE lag effect and creates 3-D structures (b) side view of etched structures in silicon, (c) side view of PDMS mold with negative replica of silicon structures, (d) side view of collagen hydrogel structures, and (e) detailed pattern transfer process *(i)* collagen transfer, *(ii)* molding, and *(iii)* stamp removal.

detailed in the previous section. The neutralized collagen was pipetted onto a coverslip with a strip of cured PDMS providing support on both sides (Figure 3-1e *(i)*). The PDMS stamp was placed on the supports to allow the excessive collagen solution to escape (Figure 3-1e *(ii)*). After devices were incubated to form the hydrogel, they were transferred to a sterile hood. In the next step, the PDMS supports were held downward with tweezers tips while the PDMS stamp was being removed upward from the pin (Figure 3-1e *(iii)*). The devices were then submerged in EGM2 cell culture media and kept in the incubator.

3.3 Results

In order to demonstrate the applicability of our recent fabrication technique to transfer patterns from silicon to collagen hydrogel, three different structures along a single microchannel were fabricated. These structures protrude from the sides of the channel, each with various length and a gradual change in the slope. Figure 3-1a shows the top view of the mask designed for this purpose. Figure 3-2a–c and Figure 3-2k–m *(i)* show the optical profilometry images of the top and side view of the fabricated structures in silicon. As shown in the side view images, *Structure a* (labelled as S *a*) is the shortest and steepest, *Structure b* (S *b*) is longer with a steep and gradual slop and one visible scallop, and *Structure c* (S *c*) is the longest, with gradual slopes and multiple scallops. Figure 3-2d shows the scanning electron microscopy (SEM) image of the tilted, top view of the PDMS channel with the 3-D structures on the side that was fabricated utilizing soft lithography from the silicon master device.

Next, these PDMS-defined patterns were transferred into type I collagen hydrogel. In order to test the cell-compatibility of the fabricated structures and observe the interaction of cells with the construct, HUVECs were seeded with EGM2 media on top of the hydrogel structures and were kept in the incubator for two days until confluency. Figure 3-2e–j and Figure 3-2k–m *(ii & iii)* juxtaposes top and side views utilizing the z-stack feature of confocal microscopy (Carl-Zeiss, LSM 510, Germany) images of 3-D collagen hydrogel devices with and without HUVECs on the structures. Collagen fibers (red), VE-Cadherin (green), nuclei (far-red), and actin (blue) were stained. As the top image of silicon structures, Figure 3-2a–c, shows the presence of window openings in the photomask has created scallops, which have been transferred to the PDMS mold utilizing soft lithography. Although scallop effects are not visible on collagen fibers, the side view

of images distinctly shows that there is a shift in the magnitude of the slope as the size of the photomask windows changes similar to those in the side view image of silicon structures.

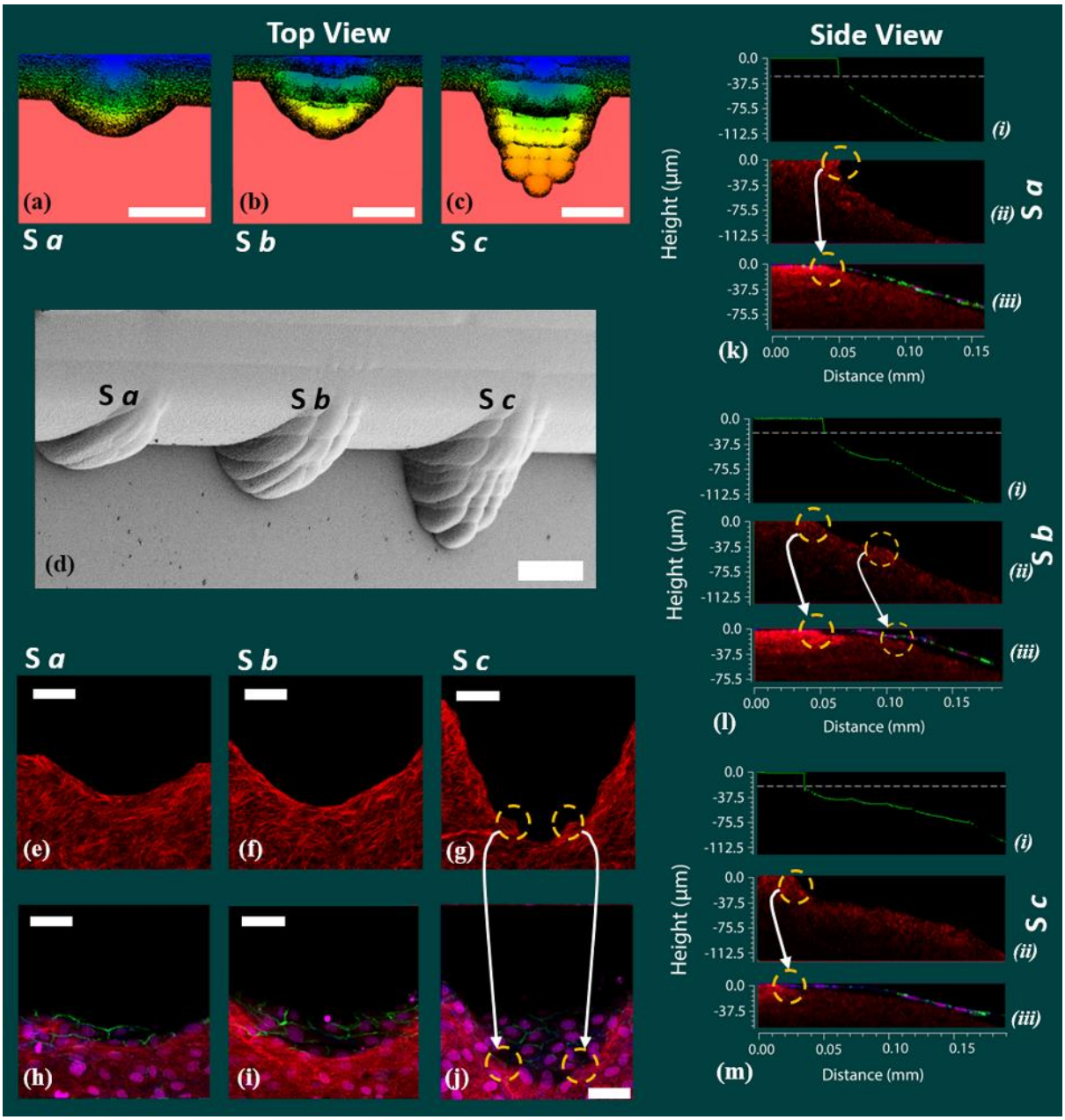

Figure 3-2 (a-c) Top optical profilometry images of silicon devices for *Structures a, b,* and *c*; scale bar: 100µm, (d) top, titled SEM image of PDMS stamp containing the negative replica of silicon structures; scale bar: 100µm, (e-j) top view of 3-D collagen fiber structures for *Structures a, b,* and *c* before and after cell patterning; scale bar: 50µm (k-m) side view of 3-D structures in (*i)* silicon, *(ii)* collagen hydrogel, and *(ii)* collagen hydrogel after cell seeding for *Structures a, b,* and *c*. The arrows indicate the site of cellular remodeling on collagen hydrogel devices.

3.4 Discussion

This work combines the robustness of micromachining in silicon to design complex structures, with the simplicity of soft lithography to fabricate those structures in a collagen hydrogel. The fabricated devices contain structures that vary in width and depth, resulting in geometries with both steep and gradual changes in slope within a continuous hydrogel. The comparison between the top and side view of the original 3-D structures in silicon (Figure 3-2a–c) and (Figure 3-2k–m *(i)*) and collagen fibers (Figure 3-2e–g) and (Figure 3-2k–m *(ii)*) shows a clear pattern fidelity between the fabricated structures. It also shows that features as small as 25µm, as depicted in Figure 3-2 can be transferred to the collagen hydrogel. Our future work will determine the minimum resolution achievable with this technique. Using profilometry and confocal imaging analysis, we determined that the dimensions of the final hydrogel structures are very close to those of the silicon structure with a maximum of 4% ± 7% difference. Such variations could be attributed to distorting hydrogel during the manual stamp removal as well as the possible stress relaxation of the soft hydrogel around the sharp corners.

The comparison between the collagen fiber images before and after cell culture reveals that the original structures are modified by cell-ECM interactions (Figure 3-2e–j) and (Figure 3-2k–m *(ii & iii)*), suggesting that cell-induced alterations in tissue structure are a critical regulator of practical biofabrication resolution that must be considered. In (S *a*), (S *b*), and (S *c*), the original structure is reduced in critical feature size from 123µm to 101µm, 80µm, and 67µm, respectively. This suggests that cells had compressed the structures to a higher extent where they were patterned on surfaces with a lower degree of slope change. For instance, near the top surface of (S *c*), endothelial cells have modified the microstructure shape *via* alteration of local fiber structure (Figure 3-3a–b). Furthermore, Figure 3-2g–j, Figure 3-2k *(i & ii)*, and Figure 3-2k *(i & ii)* show the extent of the remodeling of sharp scallops in collagen hydrogel after cell patterning.

These results indicate that 3-D structures fabricated in collagen hydrogel resemble the original structures in silicon, and highlight the dynamic interplay between the ultimate resolutions of tissue patterning resulting from cellular interaction with novel complex structures. The presented technique can pave the path to conveniently fabricate biomimetic structures in order to study cell-cell and cell-ECM interaction in a microenvironment with features that closely mimic the native tissue microstructures, and also emphasize the importance of understanding cell-induced

modification of patterned hydrogel structures as these have both technological as well as biological implications.

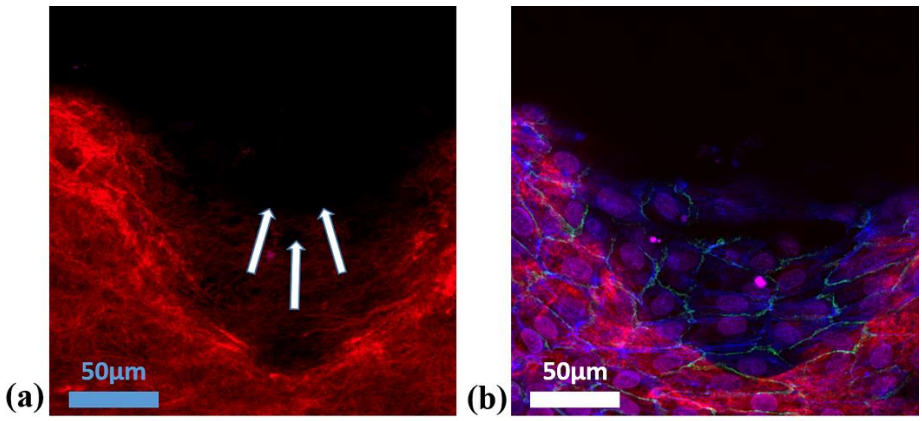

Figure 3-3 Top collagen fiber view of *structure c*, (a) without endothelial cells 6µm down the top surface and (b) with endothelial cells on top of the surface. The arrows indicate the location of altered fibers and the direction of their movement.

Chapter 4. Endothelial Cell Sensing, Restructuring, and Invasion in Collagen Hydrogel Structures

This chapter is reprinted from [86] with permission from The Royal Society of Chemistry.
Y. Hosseini, M. Agah, and S.S. Verbridge, "Endothelial cell sensing, restructuring, and invasion in collagen hydrogel structures," *Integrative Biology*, 2015.

4.1 Introduction

Angiogenesis is the formation of new blood vessels from the existing vasculature [87]. In this process, ECs lining the blood vessels sprout new capillaries into surrounding ECM, with a high degree of coordination among different EC cell subsets, *e.g.* tip and stalk cells, orchestrated by tightly regulated biochemical signaling. In wound healing, once this process is complete, the neo-vessel formation is inhibited, while in tumor microenvironments, unchecked molecular signaling can be responsible for tumor growth and dissemination, supported by a continuous growth of blood vessels into the tumor site. In this regard, the role of molecular signaling driven by soluble proteins such as vascular endothelial growth factor (VEGF), fibroblast growth factor (FGF), and platelet-derived growth factor (PDGF) family has underpinned the standard paradigm of tumor angiogenesis and the angiogenic switch, when the tumor environment overexpress pro-angiogenic growth factors to attract new blood vessels toward itself [88-91]. However, recent evidences suggest that mechanical cues likely play an equally important role in several aspects of tumor progression.

Mechanical cues such as matrix density, pore size, and fiber thickness regulate many cell behaviors. A dense matrix of fibrous collagen indicates a high risk for breast cancer metastasis [92, 93]. Small pores permit cell attachment and faster but limited cell motility, whereas large pores are better suited for long-range cell motility [94, 95]. Furthermore, the roles of matrix stiffness and pore size have previously been studied independently. It has been shown that decreasing the confinement size by decreasing the channel width for a given ECM stiffness enhances the cell migration, while increasing the ECM stiffness increases the cell migration through the same confinement effect [96]. However, the independent effects are a challenge to

decouple and the exact role of more complex aspects of the ECM structural microenvironment remains unclear.

In terms of substrate topography, studies have shown that the cell migration speed and direction depend on the curvature of the surface [97]. Geometrical cues play a role in determining the position of new branching sites from pre-existing mammary epithelial cells [98] and tumor cell invasion has been investigated from different positions within mammary ducts [99]; however, the relevance to tumor vascular networks, which are characterized by complex branching structures, has not been demonstrated clearly. Moreover, blood vessel diameters in tumor environments are uneven and vary in size abruptly and abnormally compared to those in healthy blood vessels [100]. In our previous work, we have observed that local ECM cues in certain contexts may override more traditional chemical drivers of endothelial cell (EC) invasion, however, analyzing the mechanisms has remained a challenge due to limited ability to control the ECM topography presented to cells [101]. In addition, the mechanism by which the curvature index, which represents the topography of the basement membrane of blood vessels, impacts EC invasion has rarely been studied.

The traditional methods to study EC-tissue interactions have involved seeding cells within or on top of scaffolds made from natural ECM hydrogels (*e.g.*, matrigel, collagen, fibronectin), or synthetic polymeric scaffolds (*e.g.* poly(lactic-co-glycolic acid) (PLGA) or poly(ethylene glycol) (PEG)) [73, 102]. These platforms typically do not contain complex gradients or heterogeneity that is essential to regulate relevant cellular phenotypes such as migration or invasion. While *in vivo* studies provide a higher degree of physiological relevance, dynamic experiments are challenging. Also, generally *in vivo* models provide correlations rather than causal information regarding the role of the microenvironment in regulating invasion dynamics, due to an inability to define or tune key microenvironment parameters in living systems. Microfluidic blood vessel models can provide a high degree of physiological relevance as well as the potential for dynamic, causal studies. They have been developed using either lithographic top-down or sacrificial methods to define template channels coated with ECs as biomimetic vessels; however, these studies have been mainly focused on simple structures including rectangular geometries and straight vessels [76-79].

In this paper, we have investigated the effect of different microscale topographies formed in collagen hydrogels on EC migration and capillary formation. We have fabricated a set of sharp and round structures that mimic the geometries in blood vessels such as the tube and branching sites over a wide variety of stiffness to model tissues with different mechanical properties. Our approach takes full advantage of the ability to control, with high precision, the topological microenvironment of tissues. We have furthermore characterized the cell invasion process by measuring the average sprout length and invasion frequency. Finally, we have investigated the cell-ECM interaction of ECs with sharp and round structures revealing new bi-directional regulation between the ECM microstructure and EC invasion. Such a technology will enable the *in vitro* definition, at an unprecedented spatial resolution, of 3-D tissue geometries that mimic the complex structures found *in vivo.* These platforms will enable detailed studies of the interactions between mechanical and chemical cues in tumor processes such as angiogenesis and metastasis, as well as the effect of cancer drugs in targeting these processes in a physiologically relevant context.

4.2 Materials and methods

I. Collagen hydrogel

Collagen extraction: Collagen type I was obtained from rat tail tendon under sterile condition as described previously [84]. In brief, rat tails were dissected and the tendons were extracted and processed in 0.1% acetic acid at 4^{o}C for 48 hours. The collagen solution was purified by high speed centrifugation (Avanti J-25, Beckman Coulter, CA, USA) at ×15,000g for 90 minutes. The solution was then placed at a freezer overnight and subsequently lyophilized for 48 hours until complete dryness, and kept in the freezer until right before 3-D cell culture experiments.

Collagen hydrogel preparation: Collagen hydrogel was made at the final concentration of 5mg ml^{-1}, 7.5mg ml^{-1}, and 10mg ml^{-1} from the stock solution of 7.5mg ml^{-1}, 11.25mg ml^{-1}, and 15mg ml^{-1}, respectively. This range of collagen hydrogel concentration covers the mechanical stiffness of a wide range of published normal and tumor tissues [103-105]. Desired amounts of collagen solution and the diluent media, consisting of Dulbecco's Modified Eagle's medium (DMEM) 10× (0.1 final volume neutralized collagen), NaOH (volume of collagen × 0.02), DMEM 1× (as much as necessary to adjust the final concentration), were separately prepared. The diluent media was

pipetted in the collagen solution and gently mixed with a small, sterilized spatula to avoid the formation of bubbles. Once the collagen solution was neutralized, as determined roughly by the color of the phenol red dye in the media, and confirmed with pH paper, it was dispensed on to cover glass with PDMS supports on the side, and cast against a PDMS stamp which imprinted the microstructures into the hydrogel. In order to facilitate the assembly of fiber molecules, the neutralized collagen solutions were preincubated at 4^{o}C before incubating at 37^{o}C to cross-link the fibers. As the density of collagen fibers increased, the preincubation time was also increased to allow enough time for the molecular assembly of fibers. We preincubated 5mg ml^{-1}, 7.5mg ml^{-1}, and 10mg ml^{-1} collagen solutions for 1 hour, 3 hours, and 3 hours, respectively.

II. Cell culture

Human umbilical vein endothelial cells (HUVECs) (Lonza, MD, USA) were cultured in EGM2 basal media supplemented with a growth factor bullet kit (Lonza). HUVECs were seeded at 200cells mm^{-2} on the collagen hydrogel devices between passages 3–4. After formation of a confluent monolayer on the hydrogel surface (~48 hours), hVEGF165 (10ng ml^{-1}) (Cell Signaling Technology, MA, USA) and TPA (40ng ml^{-1}) (Cell Signaling Technology) were added as they are known to promote tumor activity and angiogenesis, and furthermore to be consistent with our previous experiments [91, 101, 106]. Cell media and growth factors were changed every 48 hours during the experiment. 5mg ml^{-1}, 7.5mg ml^{-1}, and 10mg ml^{-1} hydrogel devices were fixed 48 hours, 72 hours, and 72 hours, after the addition of the growth factors (VEGF and TPA), respectively.

III. Immunofluorescence staining

Cells and collagen fibers were fixed at room temperature for 20 minutes with 10% buffered formalin (Fisher Scientific). Between each step, the samples were washed 3 times with PBS for 5 minutes each rinse. They were permeabilized by submerging in Superblock blocking buffer in PBS (Thermo Scientific) at room temperature for 2 hours while gently shaking on an orbital shaker. In the first stage, they were incubated with primary mouse monoclonal anti-collagen I (Abcam) (1:1000) and rabbit monoclonal VE-Cadherin antibody (Cell Signaling Technology) (1:250) at 4^{o}C overnight. In the second stage, they were incubated with anti-mouse Alexa Flour 546 (Life Technologies) (1:250) to stain the fibers, DAPI (Life Technologies) (1:5000) to stain the nuclei, and anti-rabbit Alexa Flour 488 (Life Technologies) (1:250) to stain cell-cell junctions at room temperature for 1 hour. To stain the actin filaments, in the second stage, cells were incubated with

Phalloidin Alexa Flour 488 (Life Technologies) (1:250) while not incubating previously with anti VE-Cadherin.

IV. ***Hydrogel structure fabrication***

The structures were fabricated in silicon utilizing deep reactive ion etching device (DRIE) (AMS 100, France), as we have previously published [71]. Utilizing soft lithography, the PDMS stamps with the negative replica of structures were fabricated. The stamps were treated with oxygen plasma (Harrick-Plasma, NY, USA), and coated with 1% bovine serum albumin (BSA) for 30 minutes at room temperature and kept on ice under sterile conditions in a biosafety cabinet, to make the PDMS surface non-adhesive to collagen hydrogel. Neutralized collagen solutions with final concentration of 5mg ml^{-1}, 7.5mg ml^{-1}, and 10mg ml^{-1} were made from concentrated collagen stock solutions and kept each on separate microtubes on ice. The BSA from the PDMS stamps was aspirated and replaced with a ~50µL drop of neutralized collagen. As 7.5mg ml^{-1} and 10mg ml^{-1} collagen solutions are highly viscous, when the collagen drops are poured on the PDMS structures, there might be air trapped that forms bubbles between the PDMS structures and collagen hydrogel interface. To remove these potential bubbles from the structures and hydrogel drops, 7.5mg ml^{-1} and 10mg ml^{-1} hydrogel devices were placed on a beaker filled with ice. The beakers were sealed with perforated parafilm, and placed under vacuum for about 2 minutes. Then, the neutralized collagen solution is pipetted on to a coverslip with two strips of PDMS support on both sides to hold the collagen solution and the PDMS stamps with structures were cast against the collagen solution.

V. ***Cell invasion characterization and analysis***

The cell invasion progress was monitored and captured by live imaging utilizing an inverted optical microscope (Axio Observer.Z1, Carl-Zeiss) equipped with an incubation chamber with a 10× objective lens. Each hydrogel device was imaged right before cell seeding, and at 24 hours intervals afterwards until fixation. In order to characterize the cell invasion progress from the structures of interest, we measured cell invasion frequency and cell invasion length utilizing Zen Lite 2012 software (Carl-Zeiss). The number of sprouts was counted from each structure (from the tip to the edge of structures). Structures with no sprouts were included in the measurement purposes with zero count. Cell invasion length was measured by the ruler feature of the Zen Lite software. Since the cells are lying on the sidewall of the microchannel, the aforementioned

parameters could be simply measured as they were imaged from the top utilizing the inverted optical microscope.

VI. Statistical analysis

The cell invasion frequency and average length were expressed as mean with the standard error of mean (SEM). One-way ANOVA with Tukey's honest significant difference (JMP Software) was performed to find significant differences between the cell invasion length results. The chi-square test with Poisson distribution (JMP Software) was performed to find significant differences between the cell invasion frequency results. Differences were considered statistically significant for (***$p < 0.001$, **$p < 0.01$, and *$p < 0.05$) with a level of significance $\alpha = 0.05$.

4.3 Results

I. Collagen hydrogel structure fabrication

Three sets of round and sharp structures with different curvature and sharpness indices were designed and fabricated in the collagen hydrogel. The curved structures are comprised of semi-elliptic structures with minor *(b)* and major radii *(a),* with the corresponding curvature indices of b/a^2 and a/b^2 on the tip and side of the structures, as shown in Figure 4.1a. On the other hand, the sharp structures are comprised of flat surfaces on the sides while intersecting each other with an angle (θ) on the tip as shown in Figure 4.1b. As shown in Figure 1a and b, cells were seeded on the structures, along with the top and bottom of the channels. Cells on the curved structures sense the curvature index between b/a^2 and a/b^2, and on the sharp structures sense the flat surfaces with an angle (θ) on the tip. Table 4.1 provides the dimension, curvature index, and angle of the fabricated structures. **Topography a** contains round (**Ra**) and sharp (**Sa**) structures with x = 100μm and y = 50μm, **Topography b** contains round (**Rb**) and sharp (**Sb**) structures with x = 100μm and y = 125μm, and **Topography c** contains round (**Rc**) and sharp (**Sc**) structures with x = 100μm and y = 250μm. The spacing between adjacent structures in all topographies is 150μm. Each device contains five topographies from each set of round and sharp structures docked along a 500μm-wide and a 95μm-deep microchannel (Figure 4.2a–c).

Furthermore, Table 4.2 shows the polymerization conditions of hydrogel devices with different concentrations, as well as the depth of the hydrogel microchannel, and fabrication yield. The depth of the hydrogel channel was calculated by seeding fluorescent microbeads on the hydrogel devices,

and measuring the difference between the point of focus of microbeads on the top and the bottom of microchannels by using an inverted microscope (Axio Observer.Z1, Carl-Zeiss, Germany). For cell seeding experiments, we used collagen hydrogel topographies whose curvature and sharpness indices were within 10% of those of the silicon template. As shown in Table 4.1, the yield for 5mg ml^{-1} concentration was 70% while yields for 7.5mg ml^{-1} and 10mg ml^{-1} were more than 90%.

Table 4-1 Dimension of fabricated structures and the curvature and sharpness index of round and sharp structures.

		a	***2b***	**axial ratio (a/*b*)**	**angle (θ) / curvature index (C.I.)**
Topography a	*Sharp a (Sa)*	100µm	50µm	4	θ = 28°
	Round a (Ra)				C.I. min= 0.0025, max=0.16
Topography b	*Sharp b (Sb)*		125µm	1.6	θ = 65°
	Round b (Rb)				C.I. min= 0.0062, max=0.025
Topography c	*Sharp c (Sc)*		250µm	0.8	θ = 100°
	Round c (Rc)				C.I. min= 0.0064, max=0.0125

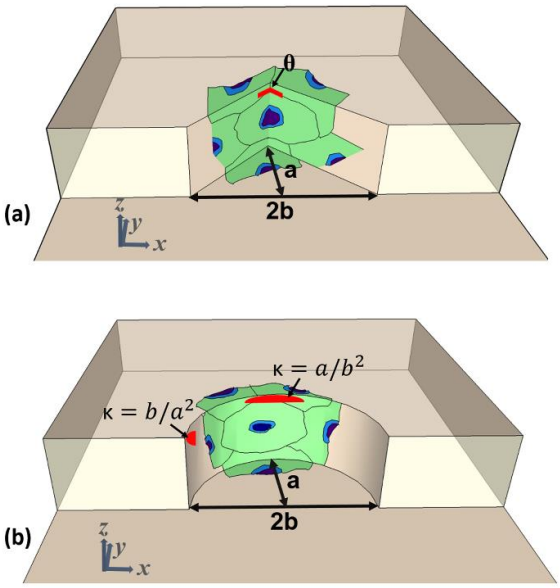

Figure 4-1 Orientation of seeded cells and dimensions of fabricated structures on (a) sharp and (b) curved structures.

Table 4-2 Summary of fabrication parameters and conditions of hydrogel structures for different stiffness. Yield was determined as the percentage of hydrogel devices fabricated within 90% pattern transfer accuracy from the original silicon structures.

	5mg ml^{-1}	**7.5mg ml^{-1}**	**10mg ml^{-1}**
Mold treatment	No treatment	Under vacuum	
Polymerization Pre-incubation Incubation	 4°C for 1 hour 37°C for 1 hour	 4°C for 3 hours 37°C for 1 hour	
z (depth) = **(measured D, SD)**	67.7µm, 6.8µm	71.7µm, 3.9µm	68.8µm, 3.1µm
Yield (within 10% limit)	~70%	~90%	~90%

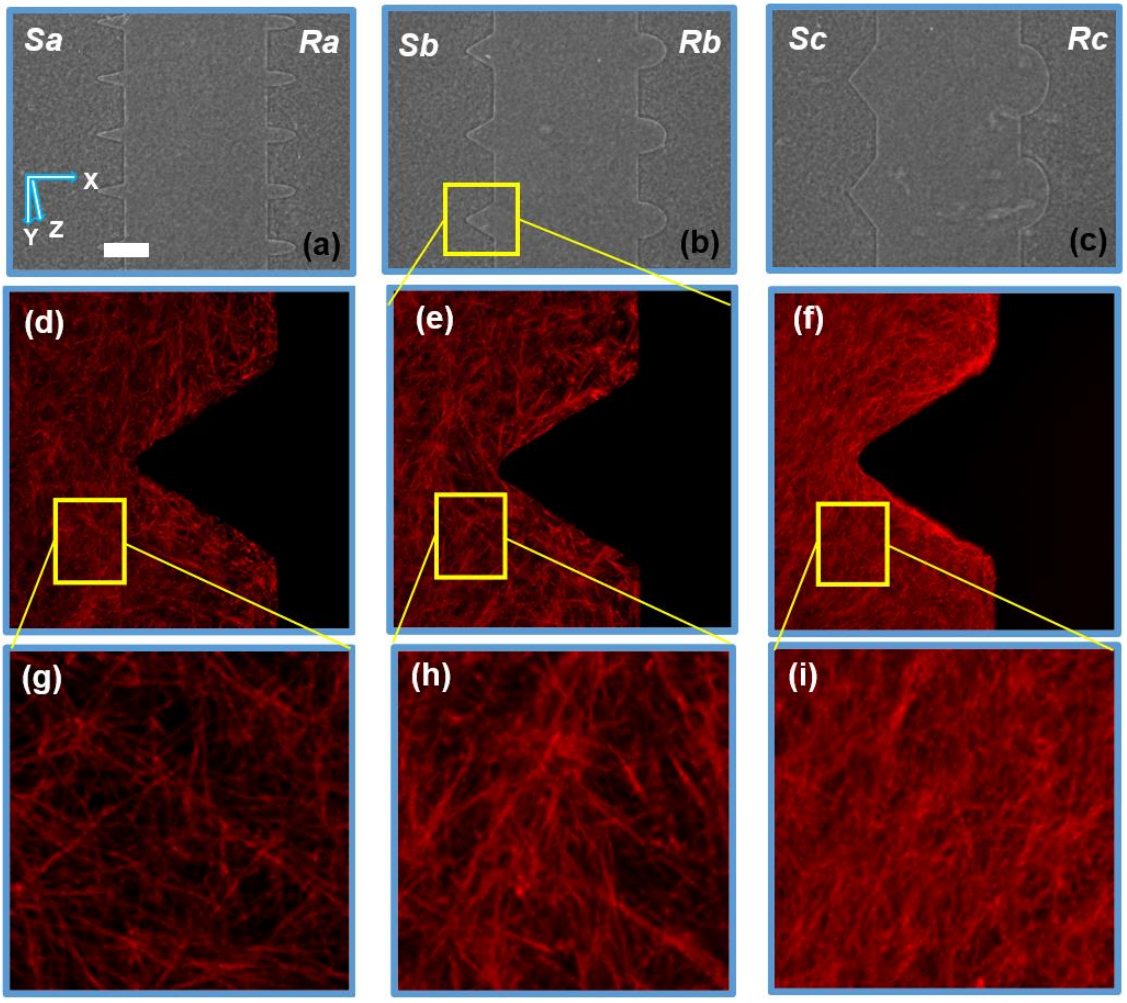

Figure 4-2 Micrographs of fabricated structures in 7.5mg ml^{-1} collagen hydrogel for structures (a) *Sa* and *Ra*, (b) *Sb* and *Rb*, and (c) *Sc* and *Rc*, and the confocal images of collagen fiber orientation around *Sb* for (d) 5mg ml^{-1}, (e) 7.5mg ml^{-1}, and (f) 10mg ml^{-1} hydrogel devices utilizing an 25× objective lens, and zoomed-in view of collagen fibers of (g) 5mg ml^{-1}, (h) 7.5mg ml^{-1}, and (i) 10mg ml^{-1} hydrogel devices.

II. Cell sensing and remodeling of collagen hydrogel

Figure 4.3 shows the confocal images of structures **Sa**, **Sc**, **Ra**, and **Rc** with developed neo-vessels from the tip of the structures. We note that in all four images, the neo-vessels were formed from the regions having higher curvature or sharpness indices. These parameters were chosen so that cells sense structures with a wide range of sharpness (from flat surfaces to sharp angels) and curvature (semi-ellipse structures with various curvature indices). Figure 4.4a and b show the micrograph of structure **Sa** right after fabrication and 3 days after fabrication without the presence of cells. The structures have not shown any sign of degradation. Figure 4.4c shows the micrograph of the same structures with cell seeding after 3 days (1 day after the addition of growth factor). The cell-cell attachment has started to deform the junctions and sides of the structures. In more detail, Figure 4.4d–f show this phenomenon imaged with the confocal microscopy. These images show structures **Sa**, **Sb**, and **Sc** (collagen fibers shown in red) 1 day after the addition of the growth factors to the cell media with overlay images of the hydrogel structures before cell culturing (collagen fibers shown in white). As the images suggest, the ECM has been deformed from the

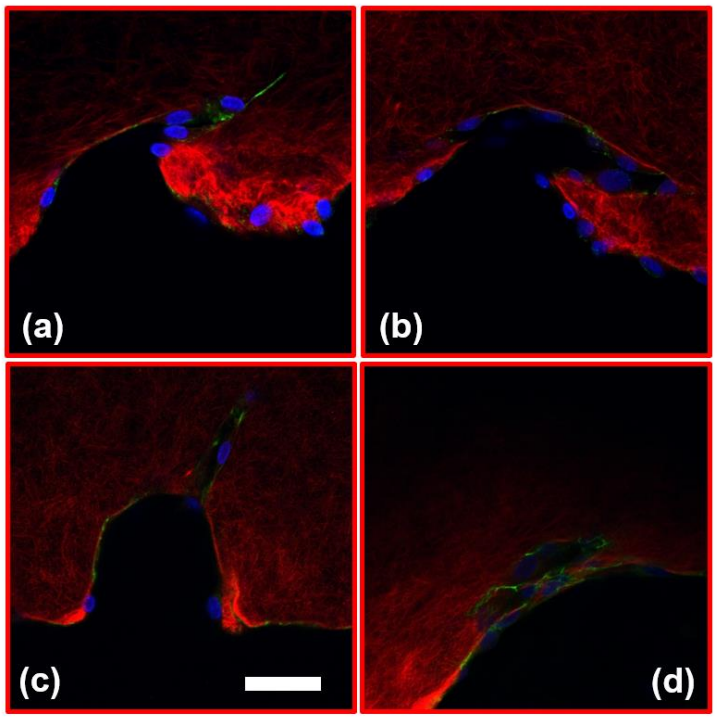

Figure 4-3 Confocal images of cell invasion through collagen hydrogel structures for structures (a) *Sa*, (b) *Sc*, (c) *Ra*, and (d) *Rc*. [red: collagen fibers, blue: nuclei, and green: VE-Cadherin]. scale bar: 50μm.

end sides resulting in an increase in the collagen fiber density at those locations (saturated red color). The structures with the highest sharpness and curvature indices have suffered larger alteration of collagen micropatterned structures (shown with green arrows).

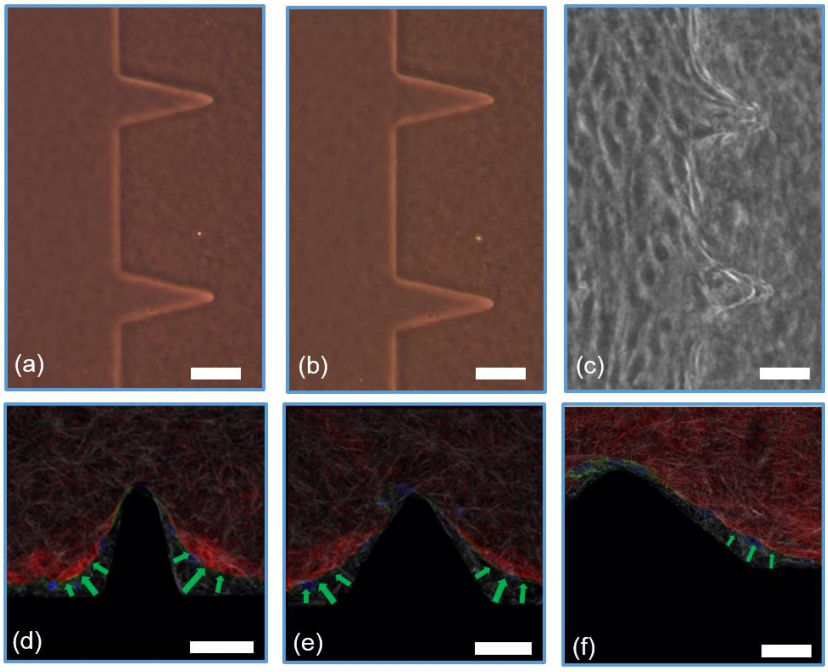

Figure 4-4 Micrograph of 7.5mg ml^{-1} collagen hydrogel structures (a) after fabrication, (b) 3 days after fabrication, (c) 3 days after cell seeding (1 day after the addition of growth factors). The confocal images of hydrogel structure deformation by cell-cell traction forces on the edge of structures for (d) *Sa*, (e) *Sb*, and (f) *Sc*. [red: collagen fibers after cell seeding, white: collagen fibers before cell seeding, blue: nuclei, and green: Actin]. scale bar: 50µm.

III. ***Collagen hydrogel structures mediate cell invasion***

Figure 4.5 shows the graph of the endothelial cell invasion frequency and length for the hydrogel devices. The invasion length and frequency were measured after 2 days for 5mg ml^{-1} and 7.5mg ml^{-1} devices and 3 days for 7.5mg ml^{-1} and 10mg ml^{-1} devices. For all cases, we did not find any significant difference between the invasion frequency within the same sharpness index category (*e.g.*, within **Topography a**, **b** or **c**). However, the more common trend (which was not statistically significant) was towards a higher invasion frequency for the round as opposed to the sharp

structures. To facilitate the comparison between index groups, the results from the same index category group were merged and compared with other groups (*e.g.*, **Topography a** vs. **Topography b**). For instance, in 5mg ml^{-1} hydrogel devices, we did not find any significant difference between **Sa** and **Ra**, but the invasion frequency of (**Sa** and **Ra**) was significantly higher compared to (**Sb** and **Rb**). For 5mg ml^{-1} devices (6 devices; 30 samples for each structure), we observed that cell invasion frequency was significantly higher for **Topography a** compared to **Topography b** and **c** (Figure 4.5a). For 7.5mg ml^{-1} devices (4 devices; 20 structures from each), after 2 days, cell invasion frequency was significantly higher for **Topography a** compared to **Topography b** and **Topography c** (Figure 4.5b), and after 3 days, cell invasion frequency remained significantly higher for **Topography a** compared to **Topography b** but not **Topography c** (Figure 4.5e). For 10mg ml^{-1} devices (5 devices; 25 structures from each), cell invasion frequency was significantly higher for **Topography a** compared to **Topography c** (Figure 4.5f) but not **Topography b**. The invasion lengths for 5mg ml^{-1} and 7.5mg ml^{-1} devices did not result in any significant differences between various structures (Figure 4.5c–d and g), however, these differences were significant at 10mg ml^{-1}, with the wider structures driving longer invasions (Figure 4.5h). Furthermore, it can be observed that the cell invasion length for the corresponding structures is higher from the softer hydrogel devices while they were measured at the same time point (*e.g.,* 5mg ml^{-1} and 7.5mg ml^{-1} devices after 2 days, and 7.5mg ml^{-1} and 10mg ml^{-1} devices after 3 days) (Figure 4.5c–d & g–h). As it has been shown already that softer hydrogel substrates lead to increased EC invasion [103, 107, 108], we will focus the following result and analysis sections on the EC invasion from 5mg ml^{-1} devices fixed after 2 days, and 7.5mg ml^{-1} and 10mg ml^{-1} devices fixed after 3 days. Where we have cross-compared the invasion frequency or length, we have done so using the same time-points. Figure 4.6 shows the micrograph of collagen hydrogel structures with HUVECs at final concentrations of 5mg ml^{-1}, 7.5mg ml^{-1}, and 10mg ml^{-1}. Each image includes a zoom-in inset that shows the structure of interest along with new sprouts.

*IV. **Structure sensing vs cell invasion***

As the confocal images show in Figure 4.7a–d, the round surfaces (**Ra** and **Rc**) are more favorable than sharp structures (**Sa** and **Sc**) for cell attachment. Cells on the wall of sharp structures form an arc to bypass the sharp tip whereas the cells fully sense the round structures during the initial phase of growth and proliferation. We compared the cell invasion length and invasion frequency from **Sa** and **Ra** for 7.5mg ml^{-1} devices, 2 days after the addition of growth factors, before the cell

sprouts become so long that there would be no significant difference between them for comparison (because of saturation of the average length) (Figure 4.7e *(i)* and *(ii)*). While there was no significant difference in the invasion length or frequency between the two structures, the trend was

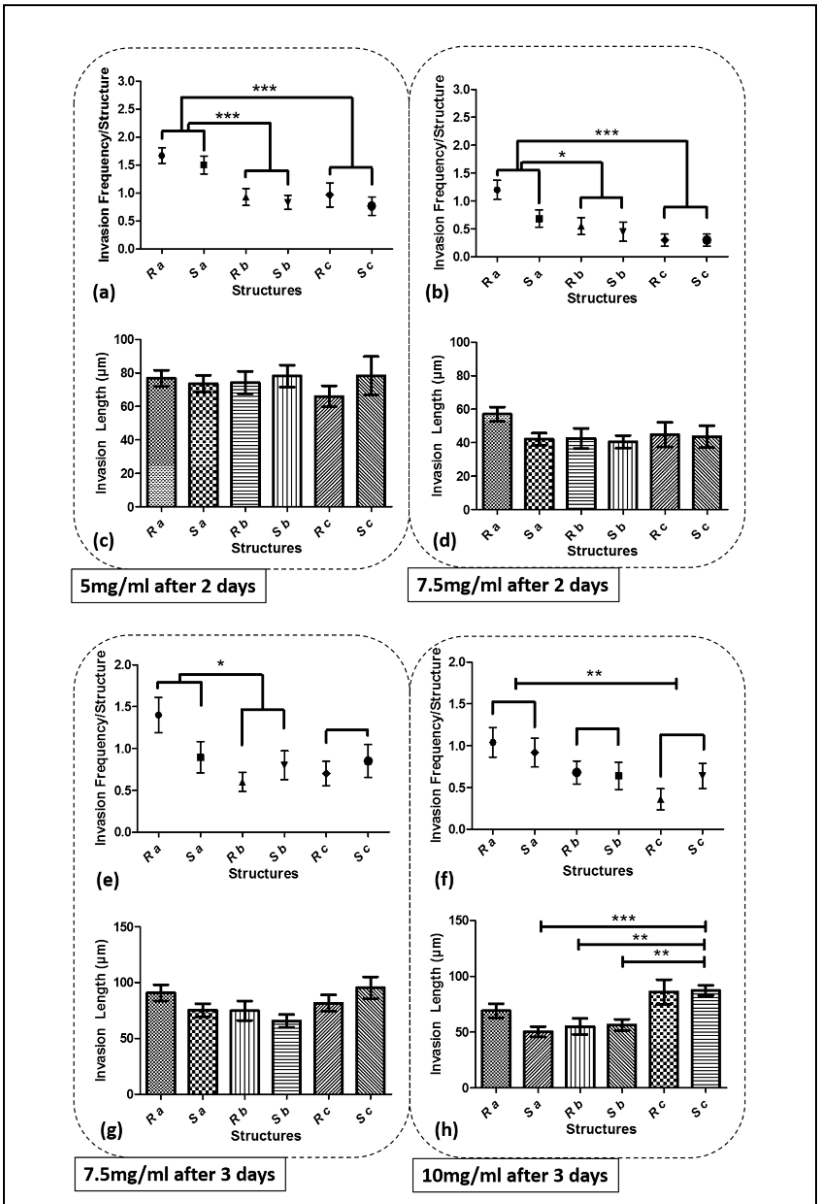

Figure 4-5 The graph of cell invasion frequency measured after 2 days for structures *Sa, Sb, Sc, Ra, Rb,* and *Rc* for (a) 5mg ml^{-1}, (b) 7.5mg ml^{-1}, and cell invasion length for the same time period and structures for (c) 5mg ml^{-1}, (d) 7.5mg ml^{-1}, and cell invasion frequency measured after 3 days for (e) 7.5mg ml^{-1} (f) 10mg ml^{-1} hydrogel devices, and cell invasion length for the same time period for (g) 7.5mg ml^{-1} (h) 10mg ml^{-1} hydrogel devices. (*** $p < 0.001$, ** $p<0.01$, and * $p<0.05$)

towards **Ra** maintaining a higher average invasion length and frequency. In order to evaluate which structures promote cell invasion faster in terms of producing longer neo-vessels, we measured the number of sprouts which were above and below average (51.8µm) for both groups (each 20 structures) since smaller neo-vessels are continuously being produced after the addition of growth factors. As shown in the graph in Fig. 4.7e *(iii)*, when analyzed in this way the round structures (**Ra**) produced longer neo-vessels than the sharp structures (**Sa**), with a statistically significant difference ($p < 0.01$).

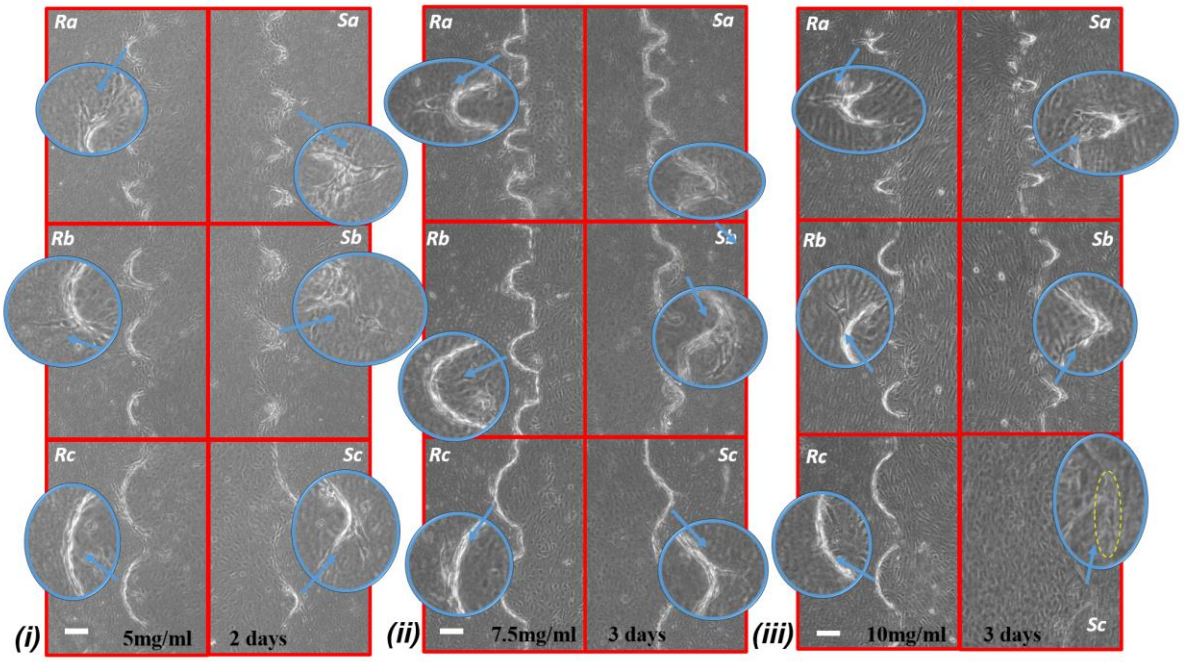

Figure 4-6 Micrograph images of cell invasion from structures ***Sa, Sb, Sc, Ra, Rb,*** and ***Rc***. for *(i)* 5mg ml^{-1} hydrogel devices, fixed 48 hours *(ii)* 7.5mg ml^{-1} hydrogel devices, fixed 72 hours, and *(iii)* 10mg ml^{-1} hydrogel devices fixed 72 hours after addition of the growth factor. In most cases cell invasion is developed from the sharp or curved tip of the structures. scale bar: 100µm.

V. Local curvature and sharpness index

Each structure within a hydrogel device consists of multiple sub-regions with different local curvature or sharpness indices. Curved structures are in fact a semi-elliptical structure with variable curvature indices along their perimeter. In **Topography a**, the sub-region with the highest curvature region is located on the tip, whereas in **structures c**, the sub-regions with the highest curvature are located on the sides. On the other hand, the sharp structures consist of side flat sub-

regions and a sharp turn on the tip. Figure 4.8a–d *(i)* show the sites of low- and high-index curved and sharp regions for **Topography a** and **Topography c**, along with the neo-vessels, which are marked with white and orange dash circles, respectively. For structures **Sa**, **Ra**, **Sc**, and **Rc**, we assumed the radius of the yellow circles centered on the tip of the structures, which represent the sub-regions of high curvature/sharpness indices to be 40µm, 40µm, 50µm, and 70µm. Outside these sub-regions, we considered that the invasion was initiated from the sub-regions with the lower curvature/sharpness index. Figure 4.8a–d *(ii)* show pie charts of neo-vessel distribution across different sub-regions of curved and sharp structures for 5mg ml^{-1}, 7.5mg ml^{-1}, and 10mg ml^{-1} hydrogel devices for **Sa**, **Ra**, **Sc**, and **Rc**, respectively. In Figure 4.5a–b & e–f, it is shown that

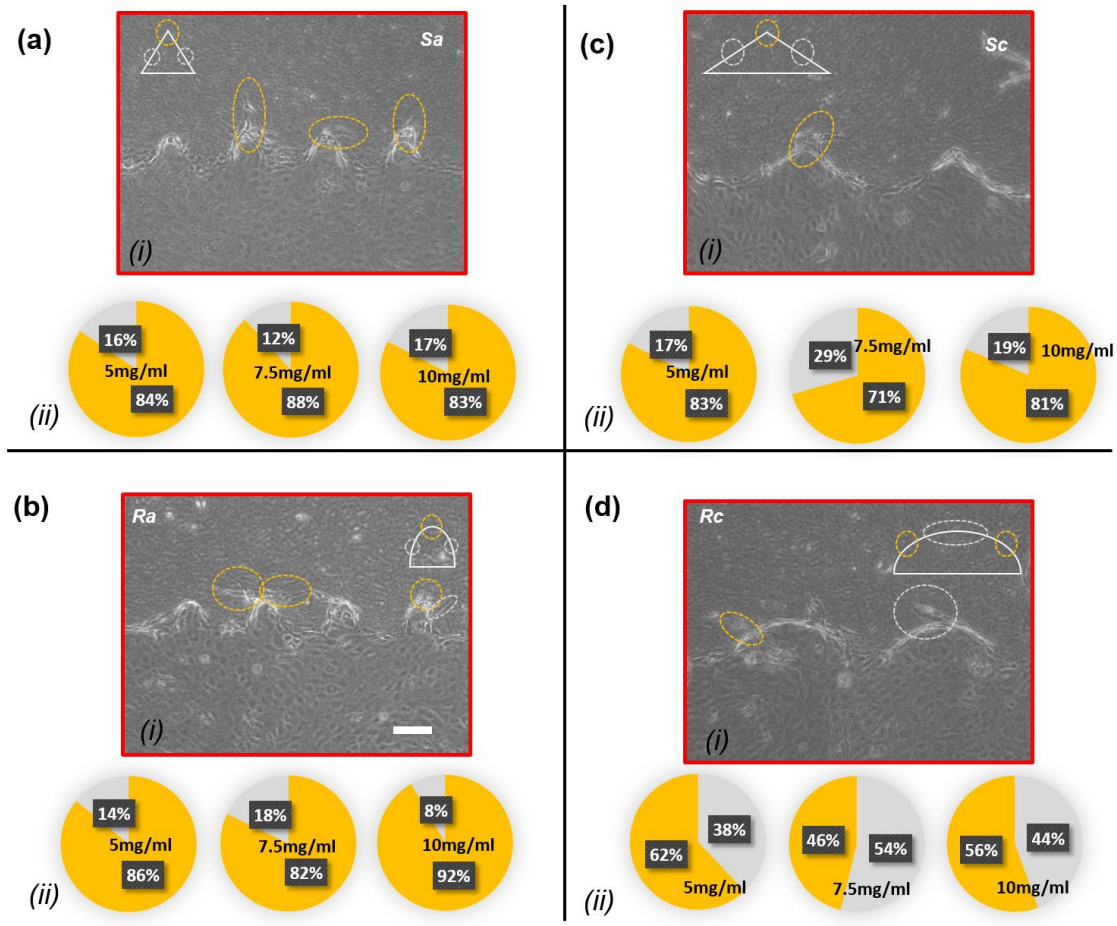

Figure 4-7 Cell invasion micrographs and confocal images with the distribution pie chart of cell invasion from different sites within each structures for (a) *Sa*, (b) *Ra*, (c) *Sc*, and (d) *Rc*. The pie chart indicates the percentile of cell invasion from high-index curved/sharp sub-regions (yellow) and low-index curved/sharp sub-regions (gray). scale bar: 100µm.

Topography a (**Sa** and **Ra**), which includes the structures with the highest curvature/sharpness index, produces more neo-vessels compared to the other topographies. Here, within the same structure group, it is shown that cell invasion is observed more from the sharper sub-regions or sub-regions with the higher curvature index. As evident in Figure 4.8a *(ii)* and b *(ii)*, on the structures **Sa** and **Sc**, the majority of neo-vessels were formed from the sharp tip of the structures. Likewise, as shown in Figure 4.8c *(ii)*, on structures **Ra**, the majority of neo-vessels were formed from the tip of the structures where the curvature index is the highest. However, in structures **Rc** the cell invasion was distributed equally across the perimeter as shown in Figure 4.8d *(ii)*.

4.4 Discussion

In this study, we have explored the interaction of ECs with sharp and curved geometries in terms of ECM sensing, remodeling and invasion. We observed the highest invasion frequency for the narrower ECM structures over all of our experiments, while this frequency was reduced at higher collagen concentrations. Both of these observations are as expected based on our prior observations of enhanced EC invasion in the sharp corners of microchannels [101], as well as observations by ourselves and others on the inhibition of EC invasion in denser hydrogel [103, 107, 108]. However, we observed a trend towards higher invasion rates for the round versus sharp structures of the same width, although this was not statistically significant. We believe this may be related to our observation that during the initial phase of cell adhesion, round structures were more favorable for cell attachment than sharp structures. We furthermore, interestingly, observed the strongest dependence of the invasion length on micro-geometry for the highest density collagen. In addition, the cell-cell attachment force on the edges of the collagen hydrogel structures deformed these structures locally. All of these latter observations suggest a balance between collagen restructuring versus invasion resulting in a complex dependence of the invasion length on the ECM density and structure.

Previous studies have shown that regions of tumor cell invasion were correlated with high mechanical stress from the tumor sites [99]. Traction forces at the invasion site have also been demonstrated to be associated with local proteolytic activity, facilitating the cancer cell invasion via matrix degradation [109, 110]. In our current work, cell-cell and cell-ECM attachments might induce such traction forces that enhance the cell invasion process in nearby structures where higher local cell density mediated by sharpness and curvature indices results in an ECM that is more

amenable to invasion. As noted previously, we observed the higher traction force adjacent to regions where we observed the higher cell invasion. In future work, the impact of such forces can be investigated by varying the geometry on the edges of the structures while keeping the curvature and sharpness indices constant where cells have previously been observed to initiate invasion.

One factor that might affect the cell invasion length among different structures is that the growth factors might not be equally distributed if the cell invasion density is not the same across all structures. For instance, it was observed that there are more cell sprouts from **Topography a** than **Topography c**, while **Topography c** maintain an even larger surface area. This means that in **Topography c**, a smaller number of cell sprouts have more room to grow while there is less competition for growth factors among the sprouts. Furthermore, the progress of cell invasion and growth of the sprouts is a continuous phenomenon that starts right after the addition of the growth factors until the cells are fixed. Therefore, the average invasion length is biased downwards by the newly formed vessels. However, the structures that promote cell invasion should contain longer neo-vessels. At early time-points, this difference might be very small, yet as time passes and the number of neo-vessels increases, there might not be any noticeable difference between the lengths of neo-vessels. Our preliminary attempts to remove this bias by binning of above versus below average length sprouts in one particular case (7.5mg ml^{-1} hydrogel devices fixed 48 hours after addition of growth factors) suggested that within one curvature and sharpness group, round structures promote cell invasion earlier in the process than the sharp structures, resulting in longer than average invasion lengths persisting at later times. The slower invasion process from these sharp structures might be attributed to the additional time and energy cells spend on remodeling and attaching to the sharp structures, and also may help explain the observed trend of higher invasion frequency for round versus sharp structures.

We have demonstrated experimentally that cell invasion frequency is dependent on geometrical cues, and geometries with the highest curvature/sharpness index produced more neo-vessels. For 7.5mg ml^{-1} devices, cell invasion frequency was significantly higher for **Topography a** (narrowest) than **Topography b** (intermediate width) and **Topography c** (widest) (Figure 4.5b) after 2 days, and for **Topography a (narrowest)** than just **Topography b** (intermediate width) after 3 days (Figure 4.5e). For 10mg ml^{-1} devices, cell invasion frequency was significantly higher for **Topography a** compared to **Topography c** (widest) after 3 days (Figure 4.5f). These results

suggest that with increasing time, the cell invasion dependency on the curvature/sharpness index decreases (Figure 4.5b and e), therefore these differences may be most relevant to early stages of sprouting and neo-vessel formation. Furthermore, we can argue that the curvature/sharpness index plays a larger role than the surface area in driving cell invasion from the stiffer substrate (Figure 4.5e and f) since **Topography c** has a higher surface area but a lower surface curvature than **Topography b**. Furthermore, as noted, we observe the largest variation in the invasion length with geometry for the stiffest ECM, *e.g.* for 10mg ml^{-1} devices the average invasion length from **Topography c** was higher compared to other structures (Figure 4.5h). These observations indicate that by increasing the mechanical stiffness of the ECM, the cell invasion dependency on curvature and sharpness configurations increases. This might be partially attributed to the low number of cell sprouts competing for cell media and growth factors within **Topography c**, however additional mechanisms related to effects such as traction forces and matrix restructuring should be examined in future work, while microfluidic channel feeding may be used to remove compounding variations in nutrition levels.

Overall, our present work provides evidence that ECs balance mechanical re-organization of the ECM structure with cellular invasion, depending on the curvature index and matrix compliance. Such a dynamic regulation of the ECM by vascular structures has not been demonstrated previously, and suggests that there may be complex feedback loops between the ECM structure and geometry and vascular dynamics that could provide therapeutic targets, or else lead to uncontrolled tumor growth if left unchecked. Our observation of enhanced dependence of the sprout length on the local ECM micro-geometry at higher versus lower tissue density may also have important implications for our understanding of the leaky, tortuous, branching, and generally highly disordered vasculature observed in dense tumor tissues. Our platforms will enable a unique exploration of the transition in EC dynamics from 2-D to 3-D geometries in terms of alteration in cell morphology and focal adhesion dynamics as well as studies of the molecular signaling regulating the observed cell dynamics.

4.5 Conclusion

In this work, we fabricated lithographically defined complex surfaces in collagen hydrogel to mimic the microstructures that vascular networks may encounter in the natural ECM. The mechanical properties of the hydrogel structures were tuned to mimic a wide range of tissues from

normal to tumor. We studied the interaction of cells with such microenvironments, which greatly impact the processes of cell proliferation, migration and development of capillary networks, all of which are significant factors in tumor neo-vascularization and growth. We found that ECs are able to fully interact with round microstructures at earlier time-points as compared with sharp ones. Furthermore, cells remodeled the microstructures with the higher sharpness/curvature index to a greater degree, and cell invasion frequency was the highest in most cases from the microstructures with the highest sharpness/curvature index. Finally, we found that dependence of the EC invasion distance on the local ECM micro-geometry was the strongest at higher matrix density. In summary, as stiffness increases from a softer to stiffer substrate, the cell invasion frequency and length decrease within the same structures. While, keeping the stiffness fixed, as the sharpness and curvature indices increase, these parameters increase. Furthermore, we showed that curved structures enhance cell invasion at early time-points. Such exploration of cell-ECM interactions and elucidation of the basic mechanisms may provide novel designs for vascular-targeting cancer treatments, and potentially improve the performance of existing anti-vascular drugs which have been a major research and investment focus.

Chapter 5. A Microengineered Boyden Chamber for Cell Migration Analysis

5.1 Introduction

Traditionally, 2-D culture systems have been widely used to study the interaction of cells with each other and biochemical reagents in culture plates, culture flasks, and petri dishes due to their ease of use and high viability of cells on 2-D surfaces [5, 6]. The first *in vitro* model developed by Boyden to study transmigration and invasion in 2-D, typically encompasses a cell culture insert housed inside a culture plate. The insert consists of a porous membrane with a predefined pore size depending on the size of cells to be monitored. Such platforms have been developed to investigate the invasion rate of lung cancer cells [8], study single tumor cell migration [9], and examine effect of specific proteins on brain cancer cells [10]. Additionally, similar platforms have been developed to increase and diversify the functionality of commercial products. For instance, the wound healing assay is utilized to measure the rate of cell migration during repair of a damaged wound [11, 12]. Spheroid migration assay [13, 14] is used to monitor the migration behavior of tumor spheroid clusters on 2-D surfaces.

With the help of microfabrication techniques, researchers have been able to miniaturize and build targeted applications for commercial *in vitro* migration and invasion assays. Utilizing soft lithography and gel injection, a microfluidic platform was developed to study the cell invasion of endothelial and cancer cells through a central channel into the side channels loaded with a chemoattractant [15, 16]. A microfluidic device with two overlaying channels separated by a commercially available 1μm-porous membrane was developed to model a vascular/valvular three-dimensional environment [17]. This platform was employed to investigate shear stress-regulated paracrine interactions between valvular endothelial cells and valvular interstitial cells. Another microfluidic device was developed in PDMS to quantify the migration and extravasation phenotype of primary tumor cells through a series of 2-D planar narrow capillary micro-channels [21]. Several other micro-based Boyden chamber devices have been developed mainly by incorporating a commercially available porous membrane to study cell migratory behaviors [111, 112].

In some of the above instances, like a Boyden chamber, cell channels are separated by a membrane or a gel layer from the chemoattractant channels. The membrane layer is cut from a commercially available transmigration well and incorporated between the custom fabricated source and chemoattractant channels, which reduces the integration capabilities of these systems as well as increases the manual labor required for fabrication. In planar devices with parallel channels, although imaging is facilitated, the throughput of the system is limited to less than two simultaneous assays.

So far, silicon has been the material of choice for micromachining. With the help of lithography and dry etching, a wide variety of structures can be fabricated in a controlled fashion, precisely on silicon substrates. DRIE has been utilized to construct deep trenches, high aspect ratio through-silicon vias [113, 114], arrays of micropillars [115] and nanowires [116]. In this setting, the etch parameters can be adjusted to control the etch rate, etch directionality, scalloping and uniformity [58, 117]. In this report, we take advantage of lithography and DRIE techniques to fabricate a versatile migration assay platform in silicon. The lithography process enables the formation of pores with different sizes and densities across a single membrane which can be used to adjust the diffusion profile. Furthermore, this work utilizes DRIE to fabricate a microfluidics-enabled deep micro-channel with a porous thin-membrane on a single silicon wafer with a high level of control on the membrane-thickness. In the future, we can take advantage of semiconductor processing techniques and silicon's electrical and mechanical properties, to investigate electrode integration for impedance sensing, improved microfluidic circulation and gradient profiles, and high throughput cell migration screening based on different candidate-drug treatment plans.

5.2 Methods

I. Cell preparations

Cell Culture: The metastatic human breast cancer cell line, MDA-MB 231 (a gift from Dr. Ayesha Shajahan-Haq, Lombardi Cancer Center, Georgetown University, Washington, DC) was obtained from American Type Culture Collection (ATCC,). Cells were maintained in T-25 flasks in Dulbecco's Modified Eagle's Medium (DMEM) (ATCC, VA, USA) containing 10% fetal bovine serum (FBS) (Atlanta Biologicals, GA, USA) and antibiotics,100 U/ml penicillin and 100 µg/ml streptomycin (Mediatech, VA, USA), at 37°C in a humidified 5% CO_2 incubator.

Cell Tagging: In order to visualize and image cells, MDA-MB 231 cells were tagged with the fluorescent tag, 5-chloromethylfluorescein diacetate (Cell Tracker Green CMFDA Dye) (Life Technologies, NY, USA). A working concentration of 5µM in serum-free media was used according to the instructions of the manufacturer.

Cell Treatments: Cells below 80% confluence were serum starved overnight in DMEM media containing no FBS. For drug treatment experiments, cells were treated with a sphingosine kinase inhibitor (SKI) compound which is known to exhibit antitumor activity [118, 119]. In order to do so, cells were incubated with the commercially available SKI compound, 5-(2-Naphthalenyl)-1H-pyrazole-3-carboxylic acid 2-[(2-hydroxy-1-naphthalenyl) methylene]hydrazide (SKI-I, ab142209) (Abcam, MA, USA). SKI-I was dissolved in dimethyl sulfoxide (DMSO) (Life Technologies, NY, USA) to make stock solutions. Aliquots were stored at -20°C for further use. SKI-I stock solution was diluted in growth medium to a final concentration of 5µM for cell treatment. Cells were incubated with the drug solution 24 hours prior to experiments and serum starved overnight.

II. Cell seeding of devices

In order to seed cells, devices were sterilized by 70% ethanol and exposed to UV overnight. Cells were harvested, suspended in serum-free media and passed through a cell strainer, Partec CellTricks (Sysmex, IL, USA), to remove cell aggregates and obtain single cell suspensions. Three separate experiments were performed; migration of serum-starved control cells towards media without serum (-FBS), media with serum (+FBS), and serum-starved SKI-I treated cells towards media with serum (SKI-I + FBS). Based on the corresponding experiment, growth medium containing no or 10% FBS was loaded into the bottom chamber of the device as a chemoattractant for serum starved cells. The cells (50,000 cells/ 200µl) in serum-free media were introduced on top of the membrane and devices were incubated at 37°C in a humidified 5% CO_2 incubator.

III. Cell viability assay

At the end of each experiment, a viability assay was performed by tagging dead cells on top of the membrane using Ethidium Homodimer-1 (EthD-1) (component B in Live/Dead viability kit for mammalian cells) (Life Technologies, NY, USA) at a final concentration of 2µM. Fluorescent images were acquired using a Zeiss Axio Imager (Germany). For each device, a representative field of view was imaged and live (green cells previously tagged with CMFDA tag) and dead cells

(red) were counted using the free public domain image processing software, ImageJ (http://imagej.nih.gov/ij/). Viability for –FBS, +FBS, and SKI-I+ FBS experiments were measured at 87.69± 2.65, 89.98± 2.76, and 83.67± 2.36 respectively.

IV. Image acquisition and analysis

Cell migration was observed by imaging the bottom side of the porous silicon membrane using a Zeiss Axio Observer.Z1 inverted epifluorescence microscope (Germany) with a 20× objective lens and imaged using a Zeiss AxioCam MRc camera (Germany). In order to obtain an overall image of the membrane, 154 frames were obtained and stitched together using the stitching utility of the Zen software. Images were acquired at 2, 6, and 12 hour time points.

ImageJ was used to analyze the acquired images. Initially a background subtract function was implemented on the images to even out the background. Afterwards images were converted to binary format using the color threshold tool in ImageJ. The particle analyze tool was used to create final masks for cell migration quantification. Artifacts and showing pores which did not contribute to the actual cell migration were removed by adjusting a size threshold of 80–110 pixels in the particle analyze tool. This threshold was determined for each experiment based on comparison with the original fluorescent image. The migration of cells in each condition was reported based on the total pixel area of the dark spots.

5.3 Results

I. Fabrication

The fabrication process flow includes the steps to fabricate the microchannel on the back and the pores on the front of a double-side polished 300 (±5) µm-thick silicon wafer as shown in Figure 5-1. The pore parameters on a high resolution chrome mask (The Photoplot Store, Co) with (r=8µm and d=50) was designed and used for lithography. In order to fabricate the pores, first, SPR 220.3 (MicroChem, MA, USA) photoresist is patterned, exposed with vacuum contact, and developed on the silicon wafer. The pores are etched using the recipe shown in Table 5-1 by an Alcatel AMS-100 DRIE (France) (Figure 5-1a). The pores are etched ~5µm more than the desired membrane thickness to ensure that they are through when the backside channel is etched. Next, a 400nm-thick silicon oxide layer is deposited utilizing a PECVD (Orion, AZ, USA) (Figure 5-1b). This oxide layer serves as a protection layer when the back-side etching of the channel meets the etched

pores. It also enables the PDMS bonding to the device by activating the O_2 groups and enhances the cell attachment to the surface by making it hydrophilic. Then, the thickness of the silicon wafer is measure utilizing a Bruker DektakXT (MA, USA). This measurement is done at this stage to minimize the contamination of silicon wafer prior to the pore fabrication. Next, the wafer is cleaned thoroughly by oxygen plasma cleaning (Trion RIE, AZ, USA) and immersing in a Nanostrip (Cyanteck, CA, USA) solution, rinsed with di-ionized (DI) water, and dried at 150^{o}C for 15 mins. Next, the microfluidic channel with a central well is fabricated on the back-side of the silicon wafer utilizing the back-side alignment and DRIE etching. The central square well and microfluidic channel are 4mm and 1mm-wide, respectively. In order to fabricate the mask, AZ9260 (AZ Electronic Materials, NJ, USA) photoresist is patented, aligned, exposed and developed. The silicon from the pore side is spun with SPR220.3 photoresist and glued to a clean silicon wafer. The second silicon wafer seals the DRIE substrate and contains the back-side cooling He gas once the pores are exposed during the channel etching.

Table 5-1 The DRIE etching parameters.

DRIE Uniform Etch Parameters		**LF Pulse Generator Parameters**		**Gas Parameters**	
ICP power	**1800 W**	**H power**	**100 W**	**SF_6 flow rate**	**300 sccm**
Chamber pressure	**$3.5e^{-2}$ mbar**	**H time**	**20 msec**	**SF_6 time**	**6 sec**
Temperature	**0^{o}C**	**L power**	**0 W**	**C_4F_8 flow rate**	**150 sccm**
He pressure	**10 mbar**	**L time**	**80 msec**	**C_4F_8 time**	**2 sec**

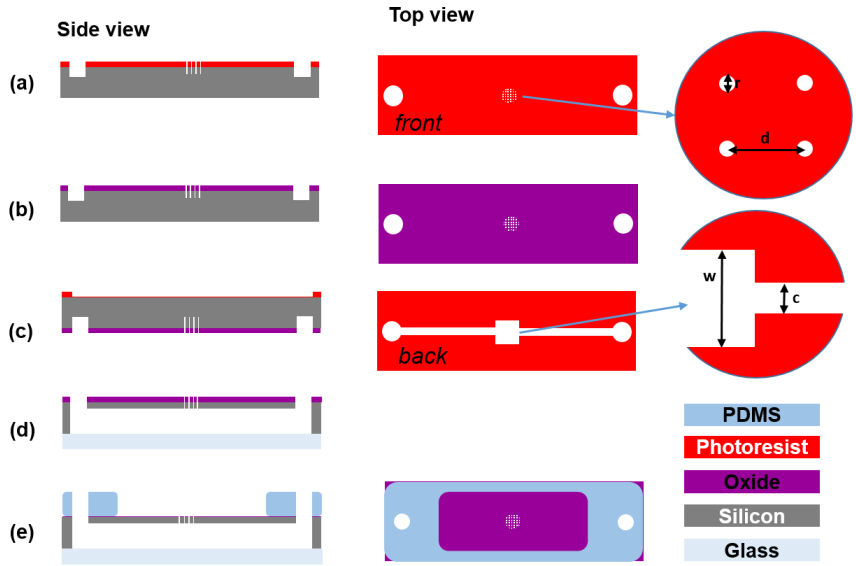

Figure 5-1 The side and top view of the fabrication process flow of deep channel and though-silicon via etching (a) Pattering photoresiste and DRIE etching of pores, (b) stripping PR and depositing the oxide layer, (c) back-side alignment and lithography of microchannels, (d) back-side channel DRIE etching and glass sealing, and (e) PDMS well bonding.

The microfluidic channels are etched using the DRIE utilizing the same recipe provided in Table 5-1. The etch rate was carefully measured at different etch points to obtain a 30µm-thick membrane (wafers etched for ~270µm). The glued wafers are immersed in a warm PRS2000 solution for 10 mins until they are detached. The devices were then cleaned (O_2 plasma and Nanostrip) and anodically bonded to a 500µm-thick Borofloat 33 glass wafer utilizing a Karl-Suss SB6 bonder (Germany) to seal the microfluidic channels. They are then diced and each individual devices are O_2 plasma-bonded utilizing a Harrick Plasma cleaner (NY, USA) to a thick PDMS with the mixture ratio of 10:1 Sylgard 184 (Dow Corning, MI, USA). Figure 5-2 shows the image of the bonded devices and ESEM images of the pores.

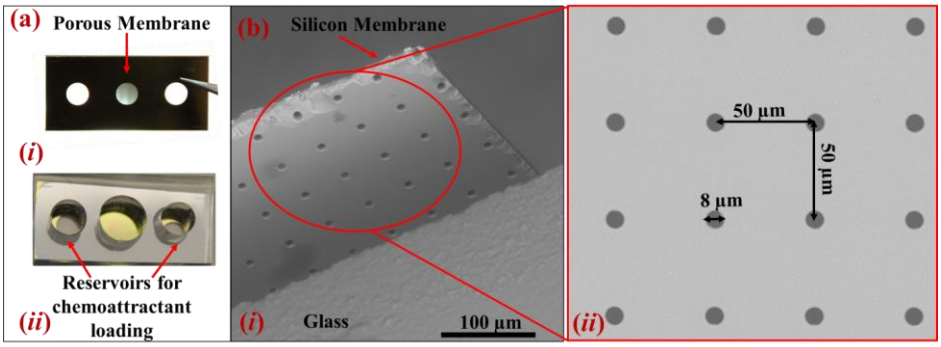

Figure 5-2 (a)(i) Final fabricated device before bonding to PDMS, (ii) final device after bonding to PDMS well, (b) (*i*) ESEM image of the overall device, (*ii*) close up image of the pores.

*II. **Experiments***

In order to verify the performance of the fabricated platform, experiments were performed as mentioned in the methods section. Figure 5-3a shows images acquired from the underside of the membrane for the different experiments at 2, 6, and 12 hour time points. Migration for each experiment is reported based on the total pixel area as mentioned in the methods section (Figure 5-3b). The final counts are shown in Figure 5-3c.

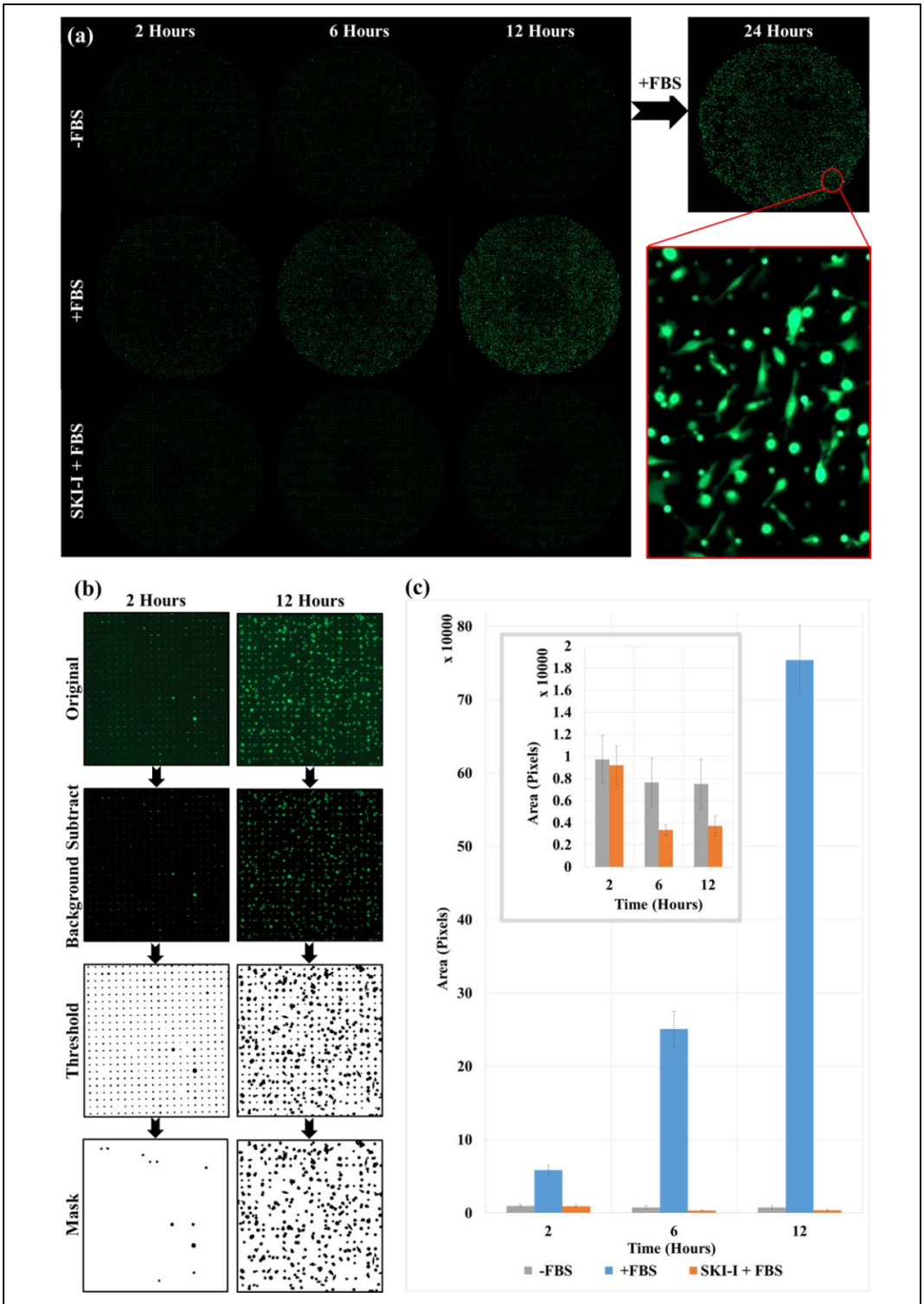

Figure 5-3 (a) Overall image of the migration membrane in –FBS (top), +FBS (middle) and SKI-I+ FBS (bottom) experiments, (b) An example of the image analysis procedure for a +FBS experiment at 2 (left) and 12 hours (right), (c) migration profile of experiments at 2,6, and 12 hour time points for 5 independent experiments represented as mean ±SEM.

Random movement and migration of the cells in the absence of a chemical gradient was studied by creating a serum-free environment above and below the membrane (-FBS experiment). Cells showed low migration after 12 hours since there was no serum available to activate a migration response in the cells. However, replacing the serum-free media below the membrane with media containing 10% FBS at the 12 hour time point and inspecting the membrane 12 hours after this change, it was evident that many cells had migrated and attached to the underside of the membrane. This phenomenon demonstrates the effective creation of a chemical gradient across the membrane and the ability of MDA-MB 231 cells to migrate through this membrane in the presence of such a gradient. Moreover, the random migration of cells which may interfere with the actual migration response caused by a chemoattractant is low in this platform. Hence further experiments were carried out to verify the function of this device to distinguish the migration behavior between normal and drug treated cells

Migration of the untreated cells in the presence of a serum gradient (+FBS experiment) was low at the 2 hour time point (Figure 5-3a). As time progressed, a clear distinction and migration was observed at the 6 hour time point and by the 12th hour the migration and attachment of cells to the underside of the silicon membrane was evident as shown in Figure 5-3a. In contrast, migration of the SKI-I treated cells showed no progress even after 12 hours. This can be an indication that the drug has affected the cells, limiting their motility and migration and making it impossible for them to get into the pores and move to the other side of the silicon membrane. Based on this observation, the fabricated device can be used to monitor and distinguish between drug treated and non-treated cells.

5.4 Discussion

Cell migration plays a key role in biological processes such as embryonic development, immune response, would healing, angiogenesis and cancer metastasis. Evaluation of the migration behavior of cells in a controlled environment is of interest to researchers as it can expand our knowledge of the signaling pathways involved in these events and the modulation of chemotactic response of cells by pharmaceutical agents. Although commercially available Boyden chambers have a polycarbonate membrane, our microfluidic migration assay was fabricated with a silicon membrane. In silicon, lithography can be used to vary the pore size and density gradually within the same device and DRIE can be used to etch the pores. This enables the evaluation of the effect

of pore size and density on cell migration under the same conditions. The silicon device can be also reused by cleaning methods that are unavailable for polycarbonate-based materials such as Nanostrip for the removal of organic materials.

In this work, we have taken advantage of lithography and DRIE techniques to fabricate a versatile migration assay platform in silicon. The lithography process enables the formation of pores with different sizes and densities across a single membrane to adjust the diffusion profile. This work furthermore utilizes DRIE to fabricate a deep microfluidics-enabled micro-channels with porous thin-membrane on a single silicon wafer with control on the membrane-thickness. Since deep etching of the back-side of the microchannel defines the thickness of the membrane, it is vital to achieve a uniform etch profile in order to fabricate the membrane with minimal thickness variation across the area that encloses the pores. Non-uniform etching will result in faster etching of the channel area than the well area which will leave the channel area thinner. If this is not checked, it might result in complete removal of the channel when etching to reduce the membrane thickness. Furthermore, a non-uniform etch profile will inadvertently produce a high level of variation on the membrane thickness across the wafer resulting in fewer usable devices. Typically, increasing the etch rate alleviates the non-uniform etching problem. We explored the effect of several parameters that affect the etch uniformity across the devices and the wafer. Reducing SF_6 etch time from 6 secs to below 4 secs in the time-multiplexed DRIE etch recipe, dramatically reduces the etch uniformity. It caused a severe reduction in etch rate on the device, especially on the outer side of the wafer. In such cases, some of the devices at the center of the wafer were etched and met the desired membrane thickness requirement, while the pores on devices at the corners were not yet visible from the channel on the back-side. The reduced etch rate also caused a non-uniform membrane with a groove-shaped pattern. The inductively coupled plasma (ICP) power, low frequency (LF) power, and temperature may also be adjusted to increase the etch rate and improve uniformity. Since the wafer is glued to a dummy wafer, temperature was not elevated and kept at 0^oC as the photoresist glue is not a good heat conductor and increased temperature might damage the contact between the two wafers. Excessive etch rate during the final phase of the etching (last 10µm) is also avoided to precisely determine the membrane thickness.

SKIs are a class of drugs with anti-tumor therapeutic potential due to their ability to inhibit tumor growth by intercepting the sphingosine kinase pathway [118]. They have been shown to have anti-proliferative effect on a variety of tumor cell lines including breast cancer cells [119].

We used the drug SKI-I to treat a highly metastatic cell line, MDA-MB-231, and used this as a model to test the working-principle of our microfluidic migration assay. Our results confirm that SKI-I causes MDA-MB-231 breast cancer cells to become apoptotic and greatly diminishes their migration through the pores in the silicon membrane. Hence, this assay is suitable for evaluating the effect of pharmaceutics and other stimuli on the migration behavior of cells.

The developed platform lends itself to the incorporation of improvements that will expand its functionality. For instance, a biocompatible hydrogel can be introduced into the top chamber to create a physiologically relevant model for cell invasion. The introduction of chemicals such as VEGF into the bottom channel can be used to create an *in vitro* model for angiogenesis. The addition of electrodes on the bottom side of the membrane, will enable automated label-free measurements of cell migration. The integration of the microchannels with porous membrane also can be used to improve microfluidic circulation and create gradient profiles across the membrane. Further, the employment of multiple stages of such blocks can result in high throughput cell migration screening based on different candidate-drug treatment plans.

5.5 Conclusion

In this work we have presented the fabrication of a silicon-based device for cell migration analysis as an alternative to conventional Boyden chamber assays. This platform integrates a porous membrane with a chemoattractant reservoir and microchannels in a single silicon wafer, reducing the number of components in a conventional Boyden chamber assay. Characterization and optimization of the microfabrication techniques with a focus on the optimization of the deep reactive ion etch parameters are presented to create porous silicon membranes with minimum thickness variance across a single membrane and between different membranes on a wafer, while controlling the pore etch rate and avoiding under/over-etching of the pores.

The experimental results we obtained from this device demonstrate its capability to detect migration towards serum in MDA-MB 231 cells. This functionality is emphasized by the fact that the cells exhibit very low migration towards serum-free media, whereas when serum is added to the same media, cells migrate to the underside of the membrane after 12 hours of no migratory activity. Moreover, the migration of drug treated cells was studied using this device. SKI-I treated

cells showed very low -close to zero- migration towards serum on this platform, exhibiting the future potential of this device to survey other potential drug treatment plans.

Chapter 6. Summary and Outlook

In brief, this dissertation so far has discussed the fabrication of bio-inspired structures in PDMS and collagen hydrogels, studied interaction of cells with ECM particularly HUVECs with a set of round and sharp structures, and demonstrated the fabrication and applicability of a silicon-based porous membrane for cell migration. The following subsection presents the summary of each chapter.

6.1 Summary of publications

I. ***A Single-Mask Process for 3-D Microstructure Fabrication in PDMS (Chapter 2)***

In this chapter, we have presented a single-mask process technique to develop 3-D structures in PDMS finding a wide variety of applications in microfluidics. This technique enables the fabrication of channels and cavities having round corners and many other customized shapes in PDMS in a predictable manner. The process relies on reactive-ion-etching lag to form 3-D channels and cavities in silicon in a single-etch process. The negative replica of patterns is then transferred from the silicon substrate to a glass master by using anodic bonding under vacuum, glass reflowing at temperatures above 700^{o}C for about 5 hours, and complete removal of silicon in KOH. Finally, soft lithography is exploited to transfer the structures to PDMS maintaining the same aspect ratio and feature sizes of the original patterns in silicon. As a case example, an insulator-based iDEP device with 3-D constrictions has been developed that can operate at lower applied potentials compared with previously reported 2-D iDEP designs. Using the 3-D iDEP device, trapping of 2-μm and 500-nm polystyrene beads was achieved with an applied potential of 150 and 350 V, respectively, with more than 80% trapping efficiency.

II. ***Bio-inspired Microstructures in Collagen Type I Hydrogel (Chapter 3)***

In this chapter, we have presented a novel technique to fabricate complex structures with varying depth and width in one single fabrication step in collagen type I hydrogel. This technique takes advantage of RIE lag to fabricate 3-D structures in silicon. Then, a PDMS replica was fabricated utilizing soft lithography and used as a stamp on collagen hydrogel to transfer these patterns. Endothelial cells were patterned on the hydrogel devices to demonstrate the applicability of this technique to define more physiologically relevant cell culture surfaces. Furthermore, confocal

microscopy was utilized to image the hydrogel devices to demonstrate the robustness of this technique before cell patterning and to study the cell-ECM interaction after cell patterning. Such patterning techniques will enhance the physiological relevance of existing 3-D cell culture platforms by providing a technical bridge between the high resolution yet planar techniques of standard lithography with more complex yet low resolution 3-D printing methods.

III. ***Geometrical Cues Mediate Endothelial Cell Invasion (Chapter 4)***

In this chapter, we have utilized collagen hydrogel to fabricate structures that recapitulate the geometries found in the basement membrane of blood vessels as well as junctions and branching sites. For this purpose, we have transferred round and sharp geometries with various curvature and sharpness index originally etched in silicon devices utilizing deep reactive ion etching technique to PDMS and collagen hydrogel utilizing soft lithography technique. Furthermore, we have cultured human umbilical vein endothelial cells on these structures to investigate the interaction between the cells and ECM. Collagen hydrogel devices were made at a wide range of stiffness to mimic different microenvironment varying from normal to tumor tissues. We have characterized cell invasion frequency and average length from the round and sharp structures. We have observed that cell invasion frequency is higher from the structures with the highest sharpness and curvature index, while in most cases the average length remain same. Also, structures with the higher invasion length is linked with the higher deformation of side structures. Furthermore, we have noted that round structures are more favorable for cell adhesion and in some cases round structures drive cell invasion faster.

IV. ***A Microengineered Boyden Chamber for Cell Migration Analysis***

In this chapter, we have presented a novel microfabricated Boyden chamber in silicon with well-defined pore sizes and controlled membrane thickness for cell migration analysis. The chip-based chamber is fabricated employing lithography and DRIE techniques on a double-side polished silicon wafer. This microdevice contains micro-pores with a silicon oxide layer at the top and a deep microfluidic channel at the bottom, which is anodically-bonded to a glass wafer for sealing and facilitating the imaging. The applicability of the chip has been demonstrated through the distinct migratory behaviors of highly metastatic breast cancer cells, MDA-MB-231, through pores with 8μm in diameter and 30μm in thickness. Utilizing this micro-based Boyden chamber device,

we have shown that MDA-MB-231 cells migrated distinctively in higher rate than MDA-MB-231 cells which had gone through SKI drug treatment over a course of 12 hours.

6.2 Contributions

As shown in Figure 6-1, this work has contributed to several research fields that altogether or partially combined can benefit a larger interdisciplinary field. We have developed the technology to fabricate 3-D MEMS devices to advance the field of tissue engineering and microfluidics. Furthermore, we have studied the interaction of cells with biomimetic ECM structures. Finally, we developed a silicon transmigration assay platform with defined pore sizes and membrane thickness. Microfluidics can be added to this platform to additionally improve the circulation profile of the device. This device can be incorporated with biomimetic hydrogel structures on top to further mimic the biomechanical cues present in the specific organ level bio-assays.

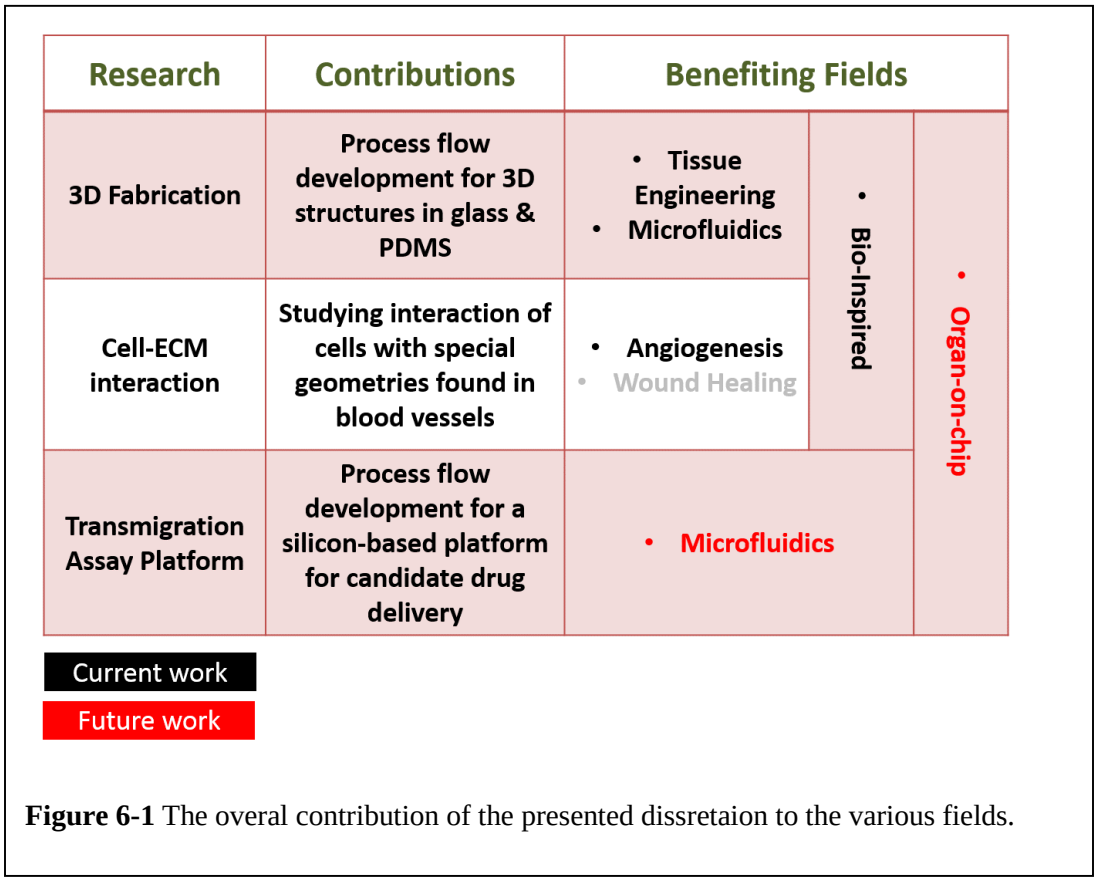

Figure 6-1 The overal contribution of the presented dissretaion to the various fields.

6.3 Future work and outlook

The future of the presented work can relies on the improvement and modification of the transmigration assay discussed in chapter 5. The implementation of this assay on a silicon substrate is beneficial for future modifications such as creating gradient profiles of the size and/or distribution of the pores, since the fabrication techniques utilized in this work are highly controllable and customizable. Additionally, the compatibility of silicon with microfabrication techniques will enable us to perform label-free detection of cell migration by integrating electrodes and sensing elements on this platform. Furthermore, microfluidics and microchannels on this device can be easily modified to create the desired chemical gradient profiles. In future, we hope to further miniaturize this platform to reduce the amount of reagents and samples needed while providing a means for high throughput assays. In addition, we will enhance the functionality of this device by adding electrodes and creating a label-free method for cell migration sensing and test other drug treatment plans with this enhanced platform.

References

[1] "Cancer Facts & Figures 2014," *American Cancer Society*, 2014.

[2] I. J. Fidler, "The pathogenesis of cancer metastasis: the 'seed and soil' hypothesis revisited," *Nature Reviews Cancer*, vol. 3, pp. 453–8, Jun 2003.

[3] P. Friedl and K. Wolf, "Tumour-cell invasion and migration: diversity and escape mechanisms," *Nature Reviews Cancer*, vol. 3, pp. 362–74, May 2003.

[4] P. Friedl and K. Wolf, "Plasticity of cell migration: a multiscale tuning model," *Journal of Cell Biology*, vol. 188, pp. 11–19, Jan 11 2010.

[5] R. R. Balcarcel and L. M. Clark, "Metabolic screening of mammalian cell cultures using well-plates," *Biotechnology Progress*, vol. 19, pp. 98–108, Jan-Feb 2003.

[6] M. Zhao, H. Bai, E. Wang, J. V. Forrester, and C. D. McCaig, "Electrical stimulation directly induces pre-angiogenic responses in vascular endothelial cells by signaling through VEGF receptors," *Journal of Cell Science*, vol. 117, pp. 397–405, Jan 26 2004.

[7] S. I. Fraley, Y. Feng, R. Krishnamurthy, D. H. Kim, A. Celedon, G. D. Longmore, *et al.*, "A distinctive role for focal adhesion proteins in three-dimensional cell motility," *Nature Cell Biology*, vol. 12, pp. 598–604, Jun 2010.

[8] W. L. Chen, K. T. Kuo, T. Y. Chou, C. L. Chen, C. H. Wang, Y. H. Wei, *et al.*, "The role of cytochrome c oxidase subunit Va in non-small cell lung carcinoma cells: association with migration, invasion and prediction of distant metastasis," *BMC Cancer*, vol. 12, p. 273, 2012.

[9] R. Harisi, I. Kenessey, J. N. Olah, F. Timar, I. Babo, G. Pogany, *et al.*, "Differential inhibition of single and cluster type tumor cell migration," *Anticancer Research*, vol. 29, pp. 2981–5, Aug 2009.

[10] S. Qi, Y. Song, Y. Peng, H. Wang, H. Long, X. Yu, *et al.*, "ZEB2 mediates multiple pathways regulating cell proliferation, migration, invasion, and apoptosis in glioma," *PLoS One*, vol. 7, p. e38842, 2012.

[11] G. J. Todaro, G. K. Lazar, and H. Green, "The initiation of cell division in a contact-inhibited mammalian cell line," *Journal of Cellular Physiology*, vol. 66, pp. 325–33, Dec 1965.

[12] C. C. Liang, A. Y. Park, and J. L. Guan, "In vitro scratch assay: a convenient and inexpensive method for analysis of cell migration in vitro," *Nature Protocols*, vol. 2, pp. 329–33, 2007.

[13] S. Krueger, T. Kalinski, H. Wolf, U. Kellner, and A. Roessner, "Interactions between human colon carcinoma cells, fibroblasts and monocytic cells in coculture--regulation of cathepsin B expression and invasiveness," *Cancer Letters*, vol. 223, pp. 313–22, Jun 8 2005.

[14] M. Vinci, C. Box, M. Zimmermann, and S. A. Eccles, "Tumor spheroid-based migration assays for evaluation of therapeutic agents," *Methods in Molecular Biology*, vol. 986, pp. 253–66, 2013.

[15] S. Chung, R. Sudo, P. J. Mack, C. R. Wan, V. Vickerman, and R. D. Kamm, "Cell migration into scaffolds under co-culture conditions in a microfluidic platform," *Lab on a Chip*, vol. 9, pp. 269–75, 2009.

[16] I. K. Zervantonakis, S. K. Hughes-Alford, J. L. Charest, J. S. Condeelis, F. B. Gertler, and R. D. Kamm, "Three-dimensional microfluidic model for tumor cell intravasation and endothelial barrier function," *Proceedings of the National Academy of Sciences of the United States of America*, vol. 109, pp. 13515–20, Aug 21 2012.

[17] M. B. Chen, S. Srigunapalan, A. R. Wheeler, and C. A. Simmons, "A 3D microfluidic platform incorporating methacrylated gelatin hydrogels to study physiological cardiovascular cell-cell interactions," *Lab On a Chip,* vol. 13, pp. 2591–8, Jul 7 2013.
[18] S. Bersini, J. S. Jeon, G. Dubini, C. Arrigoni, S. Chung, J. L. Charest, *et al.*, "A microfluidic 3D in vitro model for specificity of breast cancer metastasis to bone," *Biomaterials,* vol. 35, pp. 2454–61, Mar 2014.
[19] K. E. Sung, N. Yang, C. Pehlke, P. J. Keely, K. W. Eliceiri, A. Friedl, *et al.*, "Transition to invasion in breast cancer: a microfluidic in vitro model enables examination of spatial and temporal effects," *Integrative Biology,* vol. 3, pp. 439–50, Apr 2011.
[20] T. Liu, C. Li, H. Li, S. Zeng, J. Qin, and B. Lin, "A microfluidic device for characterizing the invasion of cancer cells in 3-D matrix," *Electrophoresis,* vol. 30, pp. 4285–91, Dec 2009.
[21] K. C. Chaw, M. Manimaran, E. H. Tay, and S. Swaminathan, "Multi-step microfluidic device for studying cancer metastasis," *Lab On a Chip,* vol. 7, pp. 1041–7, Aug 2007.
[22] M. Vinci, S. Gowan, F. Boxall, L. Patterson, M. Zimmermann, W. Court, *et al.*, "Advances in establishment and analysis of three-dimensional tumor spheroid-based functional assays for target validation and drug evaluation," *Bmc Biology,* vol. 10, Mar 2012.
[23] J. N. Heck, S. M. Ponik, M. G. Garcia-Mendoza, C. A. Pehlke, D. R. Inman, K. W. Eliceiri, *et al.*, "Microtubules regulate GEF-H1 in response to extracellular matrix stiffness," *Molecular Biology of the Cell,* vol. 23, pp. 2583-92, Jul 2012.
[24] K. Wolf and P. Friedl, "Mapping proteolytic cancer cell-extracellular matrix interfaces," *Clinical & Experimental Metastasis,* vol. 26, pp. 289-98, Apr 2009.
[25] M. Sameni, D. Cavallo-Medved, J. Dosescu, C. Jedeszko, K. Moin, S. R. Mullins, *et al.*, "Imaging and quantifying the dynamics of tumor-associated proteolysis," *Clinical & Experimental Metastasis,* vol. 26, pp. 299-309, Apr 2009.
[26] V. Brekhman and G. Neufeld, "A novel asymmetric 3D in-vitro assay for the study of tumor cell invasion," *Bmc Cancer,* vol. 9, Nov 2009.
[27] D. Huh, Y. S. Torisawa, G. A. Hamilton, H. J. Kim, and D. E. Ingber, "Microengineered physiological biomimicry: Organs-on-Chips," *Lab on a Chip,* vol. 12, pp. 2156–64, 2012.
[28] D. Huh, G. A. Hamilton, and D. E. Ingber, "From 3D cell culture to organs-on-chips," *Trends in Cell Biology,* vol. 21, pp. 745–54, Dec 2011.
[29] A. M. Ghaemmaghami, M. J. Hancock, H. Harrington, H. Kaji, and A. Khademhosseini, "Biomimetic tissues on a chip for drug discovery," *Drug Discovery Today,* vol. 17, pp. 173–181, Feb 2012.
[30] D. Huh, B. D. Matthews, A. Mammoto, M. Montoya-Zavala, H. Y. Hsin, and D. E. Ingber, "Reconstituting organ-level lung functions on a chip," *Science,* vol. 328, pp. 1662–8, Jun 25 2010.
[31] D. Huh, H. Fujioka, Y. C. Tung, N. Futai, R. Paine, 3rd, J. B. Grotberg, *et al.*, "Acoustically detectable cellular-level lung injury induced by fluid mechanical stresses in microfluidic airway systems," *Proceedings of the National Academy of Sciences of the United States of America,* vol. 104, pp. 18886–91, Nov 27 2007.
[32] A. Carraro, W. M. Hsu, K. M. Kulig, W. S. Cheung, M. L. Miller, E. J. Weinberg, *et al.*, "In vitro analysis of a hepatic device with intrinsic microvascular-based channels," *Biomedical Microdevices,* vol. 10, pp. 795-805, Dec 2008.

[33] B. J. Kane, M. J. Zinner, M. L. Yarmush, and M. Toner, "Liver-specific functional studies in a microfluidic array of primary mammalian hepatocytes," *Analytical Chemistry,* vol. 78, pp. 4291–8, Jul 1 2006.
[34] H. J. Kim, D. Huh, G. Hamilton, and D. E. Ingber, "Human gut-on-a-chip inhabited by microbial flora that experiences intestinal peristalsis-like motions and flow," *Lab on a Chip,* vol. 12, pp. 2165–74, 2012.
[35] K. J. Jang and K. Y. Suh, "A multi-layer microfluidic device for efficient culture and analysis of renal tubular cells," *Lab On a Chip,* vol. 10, pp. 36–42, Jan 7 2010.
[36] K. J. Jang, A. P. Mehr, G. A. Hamilton, L. A. McPartlin, S. Chung, K. Y. Suh, *et al.*, "Human kidney proximal tubule-on-a-chip for drug transport and nephrotoxicity assessment," *Integrative Biology,* vol. 5, pp. 1119–29, Sep 2013.
[37] Y. Zheng, J. Chen, M. Craven, N. W. Choi, S. Totorica, A. Diaz-Santana, *et al.*, "In vitro microvessels for the study of angiogenesis and thrombosis," *Proceedings of the National Academy of Sciences of the United States of America,* vol. 109, pp. 9342–7, Jun 12 2012.
[38] A. D. van der Meer, V. V. Orlova, P. ten Dijke, A. van den Berg, and C. L. Mummery, "Three-dimensional co-cultures of human endothelial cells and embryonic stem cell-derived pericytes inside a microfluidic device," *Lab On a Chip,* vol. 13, pp. 3562–8, Sep 21 2013.
[39] S. Breslin and L. O'Driscoll, "Three-dimensional cell culture: the missing link in drug discovery," *Drug Discovery Today,* vol. In Press, 2012.
[40] C. M. Nelson and M. J. Bissell, "Modeling dynamic reciprocity: Engineering three-dimensional culture models of breast architecture, function, and neoplastic transformation," *Seminars in Cancer Biology,* vol. 15, pp. 342-52, Oct 2005.
[41] J. B. Lee, M. Namgung, S. B. Lee, and S. Y. Oh, "Fabrication of an electrically conductive mixed self-assembled monolayer and its application in an electrochemical immunosensor," in *9th International Conference on Scanning Probe Microscopy, Sensors and Nanostructures,* Jeju, Korea, 2007, pp. 1352-5.
[42] G. H. Underhill, P. Galie, C. S. Chen, and S. N. Bhatia, "Bioengineering Methods for Analysis of Cells In Vitro," *Annual Review of Cell and Developmental Biology,* vol. 28, pp. 385–410, 2012.
[43] *A. Magliocco* and *C.* E*gan, Breast Cancer - Focusing Tumor Microenvironment, Stem cells and Metastasis*: InTech, 2011.
[44] Y. Hosseini, P. Zellner, and M. Agah, "A Single-Mask Process for 3-D Microstructure Fabrication in PDMS," *Journal of Microelectromechanical Systems,* vol. 22, pp. 356–62, 2013.
[45] Y. Xia and G. M. Whitesides, "Soft Lithography," *Annual Review of Materials Research,* vol. 28, pp. 153–84, 1998.
[46] A. Abbott, "Cell culture: Biology's new dimension," *Nature,* vol. 424, pp. 870–2, 2003.
[47] M.-H. Wu, C. Park, and G. M. Whitesides, "Fabrication of Arrays of Microlenses with Controlled Profiles Using Gray-Scale Microlens Projection Photolithography," *Langmuir,* vol. 18, pp. 9312–8, 2002.
[48] C. M. Waits, A. Modafe, and R. Ghodssi, "Investigation of gray-scale technology for large area 3D silicon MEMS structures," *Journal of Micromechanics and Microengineering,* vol. 3, pp. 170–7, 2003.

[49] D. Therriault, S. R. White, and J. A. Lewis, "Chaotic mixing in three-dimensional microvascular networks fabricated by direct-write assembly," *Nature Materials*, vol. 2, pp. 265–71, 2003.
[50] C. N. LaFratta, L. Li, and J. T. Fourkas, "Soft-lithographic replication of 3D microstructures with closed loops," *Proceedings of the National Academy of Sciences of the United States of America*, vol. 103, pp. 8589–94, 2006.
[51] D. Kim and P. T. C. So, "High-throughput three-dimensional lithographic microfabrication," *Optics Letters*, vol. 35, pp. 1602–4, 2010.
[52] Y. Hongbin, Z. Guangya, C. Fook Siong, W. Shouhua, and L. Feiwen, "Novel polydimethylsiloxane (PDMS) based microchannel fabrication method for lab-on-a-chip application," *Sensors and Actuators B: Chemical*, vol. 137, pp. 754–61, 2009.
[53] L. K. Fiddes, N. Raz, S. Srigunapalan, E. Tumarkan, C. A. Simmons, A. R. Wheeler, *et al.*, "A circular cross-section PDMS microfluidics system for replication of cardiovascular flow conditions," *Biomaterials*, vol. 31, pp. 3459–64, 2010.
[54] S.-H. Song, C.-K. Lee, T.-J. Kim, I.-C. Shin, S.-C. Jun, and H.-I. Jung, "A rapid and simple fabrication method for 3-dimensional circular microfluidic channel using metal wire removal process " *Microfluidics and Nanofluidics*, vol. 9, pp. 533–40, 2010.
[55] W.-C. Shih, S.-G. Kim, and G. Barbastathis, "High-resolution electrostatic analog tunable grating with a single-mask fabrication process," *Journal of Microelectromechanical Systems*, vol. 15, pp. 763–9, 2006.
[56] R. Yeh, S. Hollar, and K. S. J. Pister, "Single mask, large Force, and large displacement electrostatic linear inchworm motors," *Journal of Microelectromechanical Systems*, vol. 11, pp. 330–6, 2002.
[57] P. Zellner, L. Renaghan, Z. Hasnain, and M. Agah, "A fabrication technology for three-dimensional micro total analysis systems," *Journal of Micromechanics and Microengineering*, vol. 20, p. 045013, 2010.
[58] K. Gantz, L. Renaghan, and M. Agah, "Development of a comprehensive model for RIE-lag-based three-dimensional microchannel Fabrication," *Journal of Micromechanics and Microengineering*, vol. 18, p. 025003, 2008.
[59] G.-J. Wang, K.-H. Ho, S.-H. Hsu, and K.-P. Wang, "Microvessel scaffold with circular microchannels by photoresist melting," *Biomedical Microdevices*, vol. 9, pp. 657–63, 2007.
[60] Y.-C. Chen, G.-Y. Chen, Y.-C. Lin, and G.-J. Wang, "A lab-on-a-chip capillary network for red blood cell hydrodynamics," *Microfluidics and Nanofluidics*, vol. 9, pp. 585–91, 2010.
[61] H. Pohl, "The motion and precipitation of suspensoids in divergent electric fields," *Journal of Applied Physics*, vol. 22, pp. 869–71, 1951.
[62] R. V. Davalos, G. J. McGraw, T. I. Wallow, A. M. Morales, K. L. Krafcik, Y. Fintschenko, *et al.*, "Performance impact of dynamic surface coatings on polymeric insulator-based dielectrophoretic particle separators," *Analytical and Bioanalytical Chemistry*, vol. 390, pp. 847–55, 2008.
[63] G. J. McGraw, R. V. Davalos, J. D. Brazzle, J. Hachman, M. C. Hunter, J. Chames, *et al.*, "Polymeric microfluidic devices for the monitoring and separation of water-borne pathogens utilizing insulative dielectrophoresis," in *Proceedings of SPIE*, San Jose, CA, 2005, pp. 59–68.

[64] R. V. Davalos, G. J. McGraw, T. I. Wallow, A. M. Morales, K. L. Krafcik, Y. Fintschenko, *et al.*, "Performance impact of dynamic surface coatings on polymeric insulator-based dielectrophoretic particl sensors," *Analytical and Bioanalytical Chemistry*, vol. 389, pp. 1426–35, 2007.
[65] P. Zellner, H. Shafiee, M. Sano, R. Davalos, and M. Agah, "An Insulator-based Dielectrophoresis Silicon Microchip for Particle Trapping," presented at the Microtechnologies in Medicine and Biology, QC, Canada, 2009.
[66] W. A. Braff, A. Pignier, and C. R. Buie, "High sensitivity three-dimensional insulator-based dielectrophoresis," *Lab On a Chip*, vol. 12, pp. 1327–31, 2012.
[67] S. Ozuna-Chacon, B. H. Lapizco-Encinas, M. Rito-Palomares, S. O. Martinez-Chapa, and C. Reyes-Betanzo, "Performance characterization of an insulator-based dielectrophoretic microdevice," *Electrophoresis*, vol. 29, pp. 3115–22, 2008.
[68] J. I. Martinez-Lopez, H. Moncada-Hernandez, J. L. Baylon-Cardiel, S. O. Martinez-Chapa, M. Rito-Palomares, and B. H. Lapizco-Encinas, "Characterization of electrokinetic mobility of microparticles in order to improve dielectrophoretic concentration," *Analytical and Bioanalytical Chemistry*, vol. 394, pp. 293–302, 2009.
[69] D. Chen and H. Du, "A microfluidic device for rapid concentration of particles in continuous flow by DC dielectrophoresis," *Microfluidics and Nanofluidics*, vol. 9, pp. 281–91, 2010.
[70] R. C. Gallo-Villanueva, V. H. Perez-Gonzalez, R. V. Davalos, and B. H. Lapizco-Encinas, "Separation of mixtures of particles in a multipart microdevice employing insulator-based dielectrophoresis," *Electrophoresis*, vol. 32, pp. 2456–65, 2011.
[71] Y. Hosseini, S. S. Verbridge, and M. Agah, "Bio-inspired microstructures in collagen type I hydrogel," *Journal of Biomedical Materials Research Part A*, vol. 103, pp. 2193–7, 2015.
[72] B. V. Slaughter, S. S. Khurshid, O. Z. Fisher, A. Khademhosseini, and N. A. Peppas, "Hydrogels in Regenerative Medicine," *Advanced Materials*, vol. 21, pp. 3307–29, 2009.
[73] Y. Li, J. Rodrigues, and H. Tomas, "Injectable and biodegradable hydrogels: gelation, biodegradation and biomedical applications," *Chemical Society Reviews*, vol. 41, pp. 2193–221, Mar 21 2012.
[74] H. K. Kleinman, R. J. Klebe, and G. R. Martin, "Role of collagenous matrices in the adhesion and growth of cells," *The Journal of Cell Biology*, vol. 88, pp. 473–85, Mar 1981.
[75] E. Hesse, T. E. Hefferan, J. E. Tarara, C. Haasper, R. Meller, C. Krettek, *et al.*, "Collagen type I hydrogel allows migration, proliferation, and osteogenic differentiation of rat bone marrow stromal cells," *Journal of Biomedical Materials Research Part A*, vol. 94, pp. 442–9, Aug 2010.
[76] C. M. Kraning-Rush, S. P. Carey, M. C. Lampi, and C. A. Reinhart-King, "Microfabricated collagen tracks facilitate single cell metastatic invasion in 3D," *Integrative Biology*, vol. 5, pp. 606–16, Mar 2013.
[77] W. Bian, B. Liau, N. Badie, and N. Bursac, "Mesoscopic hydrogel molding to control the 3D geometry of bioartificial muscle tissues," *Nature Protocols*, vol. 4, pp. 1522–34, 2009.
[78] A. Golden and J. Tien, "Fabrication of microfluidic hydrogels using molded gelatin as a sacrificial element," *Lab On a Chip*, vol. 7, pp. 720–25, 2007.
[79] S. Raghavan, C. M. Nelson, J. D. Baranski, E. Lim, and C. S. Chen, "Geometrically Controlled Endothelial Tubulogenesis in Micropatterned Gels," *Tissue Engineering Part A*, vol. 16, pp. 2255–63, 2010.

[80] E. Antoine, C. Buchanan, K. Fezzaa, W. K. Lee, M. N. Rylander, and P. Vlachos, "Flow measurements in a blood-perfused collagen vessel using x-ray micro-particle image velocimetry," *PLoS One*, vol. 8, p. e81198, 2013.
[81] J. P. Morgan, P. F. Delnero, Y. Zheng, S. S. Verbridge, J. Chen, M. Craven, *et al.*, "Formation of microvascular networks in vitro," *Nature Protocols*, vol. 8, pp. 1820-36, Sep 2013.
[82] S. S. Verbridge, A. Chakrabarti, P. DelNero, B. Kwee, J. D. Varner, A. D. Stroock, *et al.*, "Physicochemical regulation of endothelial sprouting in a 3D microfluidic angiogenesis model," *Journal of Biomedical Materials Research Part A*, vol. 101, pp. 2948-56, Oct 2013.
[83] J. S. Miller, K. R. Stevens, M. T. Yang, B. M. Baker, D. H. Nguyen, D. M. Cohen, *et al.*, "Rapid casting of patterned vascular networks for perfusable engineered three-dimensional tissues," *Nature Materials*, vol. 11, pp. 768-74, Sep 2012.
[84] N. Rajan, J. Habermehl, M. F. Cote, C. J. Doillon, and D. Mantovani, "Preparation of ready-to-use, storable and reconstituted type I collagen from rat tail tendon for tissue engineering applications," *Nature Protocols*, vol. 1, pp. 2753–8, 2006.
[85] P. Zellner, L. Renaghan, and M. Agah, "A fabrication technology for three dimensional micro total analysis systems," *Journal of Micromechanics and Microengineering*, vol. 20, 2010.
[86] Y. Hosseini, M. Agah, and S. S. Verbridge, "Endothelial cell sensing, restructuring, and invasion in collagen hydrogel structures," *Integrative Biology*, Sep 17 2015.
[87] J. Folkman and Y. Shing, "Angiogenesis," *The Journal of Biological Chemistry*, vol. 267, pp. 10931–4, Jun 5 1992.
[88] G. Bergers and L. E. Benjamin, "Tumorigenesis and the angiogenic switch," *Nature Reviews Cancer*, vol. 3, pp. 401–10, Jun 2003.
[89] P. Carmeliet and R. K. Jain, "Molecular mechanisms and clinical applications of angiogenesis," *Nature*, vol. 473, pp. 298-307, May 19 2011.
[90] S. Y. Zhang, X. Bu, H. Zhao, J. T. Yu, Y. M. Wang, D. Li, *et al.*, "A host deficiency of discoidin domain receptor 2 (DDR2) inhibits both tumour angiogenesis and metastasis," *Journal of Pathology*, vol. 232, pp. 436–48, Mar 2014.
[91] A. Hoeben, B. Landuyt, M. S. Highley, H. Wildiers, A. T. Van Oosterom, and E. A. De Bruijn, "Vascular endothelial growth factor and angiogenesis," *Pharmacological Reviews*, vol. 56, pp. 549–80, Dec 2004.
[92] S. M. Kakkad, M. Solaiyappan, P. Argani, S. Sukumar, L. K. Jacobs, D. Leibfritz, *et al.*, "Collagen I fiber density increases in lymph node positive breast cancers: pilot study," *Journal of Biomedical Optics*, vol. 17, p. 116017, Nov 2012.
[93] C. E. Barcus, P. J. Keely, K. W. Eliceiri, and L. A. Schuler, "Stiff collagen matrices increase tumorigenic prolactin signaling in breast cancer cells," *The Journal of Biological Chemistry*, vol. 288, pp. 12722–32, May 3 2013.
[94] C. M. Murphy and F. J. O'Brien, "Understanding the effect of mean pore size on cell activity in collagen-glycosaminoglycan scaffolds," *Cell Adhesion & Migration*, vol. 4, pp. 377–81, Jul-Sep 2010.
[95] B. A. Harley, H. D. Kim, M. H. Zaman, I. V. Yannas, D. A. Lauffenburger, and L. J. Gibson, "Microarchitecture of three-dimensional scaffolds influences cell migration behavior via junction interactions," *Biophysical Journal*, vol. 95, pp. 4013–24, Oct 2008.

[96] A. Pathak and S. Kumar, "Independent regulation of tumor cell migration by matrix stiffness and confinement," *Proceedings of the National Academy of Sciences of the United States of America,* vol. 109, pp. 10334–9, Jun 26 2012.
[97] M.-C. Kim, C. Kim, L. Wood, D. Neal, R. D. Kamm, and H. H. Asada, "Integrating focal adhesion dynamics, cytoskeleton remodeling, and actin motor activity for predicting cell migration on 3D curved surfaces of the extracellular matrixw," *Integrative Biology,* vol. 4, pp. 1386–97, 2012.
[98] C. M. Nelson, M. M. VanDuijn, J. L. Inman, D. A. Fletcher, and M. J. Bissell, "Tissue geometry determines sites of mammary branching morphogenesis in organotypic cultures," *Science,* vol. 314, pp. 298-300, Oct 2006.
[99] E. Boghaert, J. P. Gleghorn, K. Lee, N. Gjorevski, D. C. Radisky, and C. M. Nelson, "Host epithelial geometry regulates breast cancer cell invasiveness," *Proceedings of the National Academy of Sciences of the United States of America,* vol. 109, pp. 19632-7, Nov 2012.
[100] D. Fukumura, D. G. Duda, L. L. Munn, and R. K. Jain, "Tumor microvasculature and microenvironment: novel insights through intravital imaging in pre-clinical models," *Microcirculation,* vol. 17, pp. 206–25, 2010.
[101] S. S. Verbridge, A. Chakrabarti, P. DelNero, B. Kwee, J. D. Varner, A. D. Stroock, *et al.*, "Physicochemical regulation of endothelial sprouting in a 3D microfluidic angiogenesis model," *Journal of Biomedical Materials Research Part A,* 2013.
[102] C. Fischbach, R. Chen, T. Matsumoto, T. Schmelzle, J. S. Brugge, P. J. Polverini, *et al.*, "Engineering tumors with 3D scaffolds," *Nature Methods,* vol. 4, pp. 855–60, Oct 2007.
[103] V. L. Cross, Y. Zheng, N. Won Choi, S. S. Verbridge, B. A. Sutermaster, L. J. Bonassar, *et al.*, "Dense type I collagen matrices that support cellular remodeling and microfabrication for studies of tumor angiogenesis and vasculogenesis in vitro," *Biomaterials,* vol. 31, pp. 8596–607, Nov 2010.
[104] M. J. Paszek, N. Zahir, K. R. Johnson, J. N. Lakins, G. I. Rozenberg, A. Gefen, *et al.*, "Tensional homeostasis and the malignant phenotype," *Cancer Cell,* vol. 8, pp. 241-54, Sep 2005.
[105] S. Ramanujan, A. Pluen, T. D. McKee, E. B. Brown, Y. Boucher, and R. K. Jain, "Diffusion and convection in collagen gels: Implications for transport in the tumor interstitium," *Biophysical Journal,* vol. 83, pp. 1650–60, Sep 2002.
[106] J. L. Gross, D. Moscatelli, and D. B. Rifkin, "Increased capillary endothelial cell protease activity in response to angiogenic stimuli in vitro," *Proceedings of the National Academy of Sciences of the United States of America,* vol. 80, pp. 2623–7, May 1983.
[107] C. M. Ghajar, X. Chen, J. W. Harris, V. Suresh, C. C. Hughes, N. L. Jeon, *et al.*, "The effect of matrix density on the regulation of 3-D capillary morphogenesis," *Biophys J,* vol. 94, pp. 1930-41, Mar 1 2008.
[108] M. E. Francis-Sedlak, M. L. Moya, J. J. Huang, S. A. Lucas, N. Chandrasekharan, J. C. Larson, *et al.*, "Collagen glycation alters neovascularization in vitro and in vivo," *Microvasc Res,* vol. 80, pp. 3-9, Jul 2010.
[109] A. Aung, Y. N. Seo, S. Lu, Y. Wang, C. Jamora, J. C. del Alamo, *et al.*, "3D traction stresses activate protease-dependent invasion of cancer cells," *Biophysical Journal,* vol. 107, pp. 2528–37, Dec 2 2014.
[110] R. J. Jerrell and A. Parekh, "Cellular traction stresses mediate extracellular matrix degradation by invadopodia," *Acta Biomaterialia,* vol. 10, pp. 1886–96, May 2014.

[111] E. Primiceri, M. S. Chiriaco, F. Dioguardi, A. G. Monteduro, E. D'Amone, R. Rinaldi, *et al.*, "Automatic transwell assay by an EIS cell chip to monitor cell migration," *Lab on a Chip*, vol. 11, pp. 4081–6, 2011.
[112] D. Kwasny, K. Kiilerich-Pedersen, J. Moresco, M. Dimaki, N. Rozlosnik, and W. E. Svendsen, "Microfluidic device to study cell transmigration under physiological shear stress conditions," *Biomedical Microdevices*, vol. 13, pp. 899–907, Oct 2011.
[113] M. Koyanagi, T. Fukushima, and T. Tanaka, "High-Density Through Silicon Vias for 3-D LSIs," *Proceedings of the IEEE*, vol. 97, pp. 49–59, Jan 2009.
[114] D. S. Tezcan, K. De Munck, N. Pham, O. Luhn, A. Aarts, P. De Moor, *et al.*, "Development of vertical and tapered via etch for 3D through wafer interconnect technology," in *8th Electronic Packaging Technology Conference*, 2006, pp. 22–8.
[115] H. Shakeel and M. Agah, "Semipacked Separation Columns with Monolayer Protected Gold Stationary Phases for Microgas Chromatography," in *Proceedings of the IEEE Sensors* 2012, pp. 2007–10.
[116] A. Zeniou, K. Ellinas, A. Olziersky, and E. Gogolides, "Ultra-high aspect ratio Si nanowires fabricated with plasma etching: plasma processing, mechanical stability analysis against adhesion and capillary forces and oleophobicity," *Nanotechnology*, vol. 25, Jan 24 2014.
[117] K. S. Chen, A. A. Ayon, X. Zhang, and S. M. Spearing, "Effect of process parameters on the surface morphology and mechanical performance of silicon structures after deep reactive ion etching (DRIE)," *Journal of Microelectromechanical Systems*, vol. 11, pp. 264–75, Jun 2002.
[118] K. J. French, R. S. Schrecengost, B. D. Lee, Y. Zhuang, S. N. Smith, J. L. Eberly, *et al.*, "Discovery and Evaluation of Inhibitors of Human Sphingosine Kinase," *Cancer Research*, vol. 63, pp. 5962–9, 2003.
[119] K. J. French, J. J. Upson, S. N. Keller, Y. Zhuang, J. K. Yun, and C. D. Smith, "Antitumor Activity of Sphingosine Kinase Inhibitors," *Journal of Pharmacology and Experimental Therapeutics*, vol. 318, pp. 596–603, 2006.